Master’s Degree in
Nanotechnologies for ICTs

Design and fabrication of a wireless implantable pulse generator for targeted neuromodulation of the optic nerve based on flexible, organic optoelectronics

First Advisor: Prof. Valentina Cauda
Second Advisor: Prof. Carlo Ricciardi

First Supervisor: Prof. Diego Ghezzi
Second Supervisor: Doc. Eleonora Borda

Candidate:
Giulia Mongardi

Academic Year 2018/2019

Acknowledgements

I would like to express my deep gratitude to Professor Diego Ghezzi who gave me the possibility to carry out this research work in his laboratory and for his constant scientific support.

I would like to thank Prof. Valentina Cauda and Prof. Carlo Ricciardi for giving us the opportunity to work in a host laboratory abroad and for giving us logistic support.

Thanks to all the members of LNE laboratory who have always been willing to answer technical questions and who were able to welcome me and the other students in a relaxed and friendly environment. In particular I owe my deep gratitude to Marta for her fundamental technical support and enthusiasm and to Eleonora for her timely guidance, for the weekends spent in the cleanroom together and for her friendship.

Thanks to the Wyss center staff members Anthony and Valérian for their patience and for always trying to fix my mistakes.

Thanks to the Nanotech 14 students for having been a family in Turin, Grenoble and Lausanne.

Thanks to my climbing fellows for the long weekends and climbing trips, for bearing my disorganization and for checking the weather for the following weekend on Monday mornings. Among them, a special thanks to Federico for our adventures and for his stories.

Thanks to Osteria dell'Orso and Rue Michelet 8 for having been the places where I met the most wonderful and diverse team I could wish to have during these years: Lore, Jaco, Petro, Teo and Glori.
In particular:
Thanks to Lore for teaching us to look at the world with wonder.
Thanks to Jaco for his critical thinking, for the numerous debates and for his eccentric shirts.
Thanks to Petro for the neverending phone calls and for remembering us how important it is to be together.
Thanks to Teo for being so rational and for often mitigating my profound despair.
Thanks to Glori for her sharp humor and for thousands other reasons.

Thanks to my sister Francesca and my brother Giorgio for loving me despite everything and thanks to my parents and to my grandparents for understanding the reasons that brought me abroad and for their constant encouragements.

Abstract

In the last decades neuroprosthetics has become a major field of interest for both academic research and industry. Neural interfaces can, nowadays, restore cognitive, motor and sensory primary functions such as hearing, tactile sense and vision, as well as reduce symptoms in patients affected by chronic diseases, such as Parkinson's disease. Neural interfaces, as most of implantable medical devices, rely on the presence of a battery and a pulse generator in order to deliver the pulse for activating neuronal response. However, two major issues affect this traditional power supply system: first, miniaturization of batteries while maintaining a decent lifetime is nowadays encountering a limit and, secondly, cumbersome and stiff devices can hardly interact with soft biological tissues without provoking acute and chronic inflammation. In this framework researchers are investigating novel solutions to replace such power supply system. One plausible approach would be to exploit an implanted transducer that could generate pulses for stimulation by being driven from an external module. By undertaking this path the implantable device could be designed to be totally flexible and to blend in with the biological tissues. A matrix of organic photovoltaic cells could potentially serve this purpose. As a matter of fact, photovoltaic technology can easily be thought in a flexible solution and it is prone to miniaturization. The following study has been conceived within this framework. Therefore, we propose an organic photovoltaic cells array designed as bulk heterojunction PV and based on a photo-active layer of PCPDTBT:PCBM in order to be integrated with the self-opening intraneural electrode array for targeted neuromodulation of the optic nerve for vision restoration (OpticSELINE) [1]. In the following work we explore materials suitable for building flexible photovoltaic cells working in NIR-IR wavelength range, as well as encapsulation and substrate materials for ensuring minimal inflammatory response and fibrotic capsule formation. The purpose of this work is to build a first prototype and to set a standard fabrication process to ensure materials integration and repeatability of the procedures. So far we have achieved a fair level of optimization of the process flow and nice integration between the multitude of materials implemented. Moreover, the functioning and the performances of the electrodes has been assessed via impedance spectroscopy and cyclic voltammetry. From the standpoint of the photovoltaic response, we have set a benchmark for further studies. Even though the prototypes we present in this thesis are only a small step towards the final goal, we have been able to successfully transfer an idea into a first physical device and help reducing the gap between the issue and the solution.

Keywords: neuroprosthetics, wireless implantable pulse generator, optic nerve stimulation, flexible bioelectronics, organic photovoltaic, conjugated polymers

Contents

Acknowledgement **i**

Abstract **iii**

Table of contents **vi**

List of figures **viii**

List of Abbreviations **ix**

1 Introduction **1**

2 Background **3**
- 2.1 Physiology of vision . . . 3
- 2.2 Blindness, electrical stimulation of neural tissue and visual prosthesis . . 5
- 2.3 Self-opening intraneural electrode for optic nerve stimulation (OpticSELINE) . . . 7
- 2.4 Flexible materials for compliant neuroprosthesis . . . 8
- 2.5 Energy scavenging technologies for implantable devices . . . 9
- 2.6 Organic photovoltaic devices . . . 10
  - 2.6.1 Principle of operation . . . 11
- 2.7 Purpose of the study . . . 12

3 Materials and methods **15**
- 3.1 Design . . . 15
  - 3.1.1 Measurement configurations . . . 15
  - 3.1.2 Electrodes design . . . 16
  - 3.1.3 Photovoltaic cells design . . . 18
  - 3.1.4 Substrate and encapsulation materials . . . 20
- 3.2 Microfabrication . . . 21
  - 3.2.1 First prototype process flow . . . 21
  - 3.2.2 Final prototype process flow . . . 24
- 3.3 From the first to the optimized prototype . . . 27
  - 3.3.1 Summary: from prototype 1 to prototype 4 . . . 29
- 3.4 Electrochemical characterization . . . 31
  - 3.4.1 Impedance spectroscopy . . . 31
  - 3.4.2 Cyclic voltammetry . . . 32
- 3.5 Photovoltaic characterization . . . 33
  - 3.5.1 Materials stack photovoltaic characterization through dedicated chips fabrication and testing . . . 33

4 Results and discussion **35**
4.1 Preliminary results 35
  4.1.1 Materials stack photovoltaic response 35
  4.1.2 ITO deposition for optimized sheet resistance 36
4.2 Batch 1 37
  4.2.1 Microfabrication results 37
  4.2.2 Electrochemical characterization 39
4.3 Batch 2 39
  4.3.1 Microfabrication results 39
  4.3.2 Electrochemical characterization 41
4.4 Batch 3 42
  4.4.1 Microfabrication results 42
  4.4.2 Electrochemical characterization 43
4.5 Batch 4 44
  4.5.1 Microfabrication results 44
  4.5.2 Electrochemical characterization 45
4.6 Photovoltaic characterization 46

5 Conclusion and future developments **53**

6 Appendix **59**
6.1 PEDOT:PSS + GOPS preparation 59
6.2 PCPDTBT + $PC_{60}BM$ (blend) preparation 59
6.3 OSTE+ flex preparation 60
6.4 OSTE+ CC preparation 60

List of Figures

2.1 Anatomy of human eye 4
2.2 Anatomy of human retina 5
2.3 The intraneural electrode array OpticSELINE 7
2.4 Structures of organic solar cells 11
2.5 Structure and working principle of a bulk-heterojunction organic solar cell 13

3.1 Design of the devices for electrochemical and photovoltaic experiments . 16
3.2 Photovoltaic cells configurations and related equivalent circuits 17
3.3 Electrodes design 18
3.4 Schematics of photo-active materials stack band-diagram 19
3.5 Graphic process flow: prototype 1 25
3.6 Mask design implemented for bottom layer patterning and ITO deposition 26
3.7 Mask design implemented for top layer patterning and Pt deposition . . . 27
3.8 Graphic process flow: final prototype 28
3.9 Experimental set-up for photovoltaic and electrochemical measurements 32
3.10 LED irradiance (μW/mm^2) versus bias voltage applied 33
3.11 Measurement set up for materials stack photovoltaic characterization . . 34

4.1 Photo-generated voltage and current density of one electrode of test chips for increasing LED irradiance 36
4.2 Average photo-generated voltage and current density of test chips for increasing LED irradiance 36
4.3 ITO sputtered films 4 points resistance versus pressure and temperature . 37
4.4 Bottom electrodes, batch 1: average impedance module and phase 39
4.5 Top electrodes, batch 1: impedance module and phase 40
4.6 Bottom electrodes, batch 2: average impedance module and phase 41
4.7 Top electrodes, batch 2: impedance module and phase 42
4.8 Bottom electrodes built on non-uniformly cured OSTE+ CC, batch 3: impedance module and phase 43
4.9 Bottom electrodes built on uniformly cured OSTE+ CC, batch 3: average impedance module and phase 44
4.10 Cyclic voltammetry: cathodes, batch 4 45
4.11 Charge Storage Capacity (CSC): cathodes, batch 4 46
4.12 Photo-generated voltage and current density for increasing LED irradiance: batch 4, electrode diameter equal to 1000 μm 47
4.13 Major microfabrication issues and solution: batch 1 48
4.14 Major microfabrication issues and solution: batch 2 49
4.15 Major microfabrication issues and solution: batch 3 50
4.16 Major microfabrication issues and solution: batch 4 51

List of Abbreviations

AMD	Age-related Macular Degeneration
BHJ	Bulk-heterojunction
CSC	Charge Storage Capacity
CV	Cyclic Voltammetry
GOPS	(3-glycidyloxypropyl)trimethoxysilane
HOMO	Highest Occupied Molecular Orbital
IMD	Implantable medical devices
INL	Inner Nuclear Layer
IPG	Implantable Pulse Generator
IR	Infrared
LED	Light Emitting diode
LGN	Lateral Geniculate Nucleus
LUMO	Lowest Unoccupied Molecular Orbital
MEA	Multielectrode array
MLA	Maskless Aligner
NIR	Near infrared
OPV	Organic Photovoltaics
OSTE+ CC	OSTEMER^{TM}322 Crystal Clear
OSTE+ flex	OSTEMER®324 Flex
PDMS	polydimethylsiloxane
PCPDTBT	Poly4,4-dialkyl-4H-cyclopenta[2,1-b;3,4-b]dithiophene-2,6- diyl-alt-2,1,3-benzothiadiazole-4,7-diyl
PEDOT:PSS	Poly(3,4-ethylenedioxythiophene) polystyrene sulfonat
PI	Polymide
PC	Photo-current
PV	Photo-voltage
RGC	Retinal Ganglion Cell
RIE	Reactive Ion Etching

RP	Retinis Pigmentosa
RPE	Retinal Pigment Epithelium
SEM	Scanning Electron Microscopy
SIROF	Sputtered Iridium Oxide Film

1 Introduction

In the last few decades, along with a steady development in electronics and microfabrication techniques, a significant progress has been made in the field of neuroprosthetics. Nowadays neural prostheses enable to restore fundamental sensory, motor and cognitive functions and to improve the overall quality of life of patients affected by chronic diseases. In particular, the miniaturization of devices has allowed in-vivo implantation for multiple purposes, such as diagnosis, monitoring and therapy. Researchers are currently working to improve design, performances and portability of these devices and are studying novel solutions to restore primary functions of human body, e.g. visual prostheses, cochlear implants, spinal cord stimulation interfaces [2; 3].

Although these innovations have gradually helped to enhance quality of life, they still suffer from some major issues. Generally, active implantable medical devices (IMDs), among which also neuroprosthetic interfaces, rely on primary Lithium-based batteries. Being non-rechargeable, they must be replaced when spent. This constraint obliges patients to undergo new surgeries after the first implantation. Together with the intrinsic risks for the patient, multiple surgeries lead to higher costs of hospitalization. Standard implanted pacemakers could reach a lifetime of 10 to 15 years [4], but the lifespan of implantable cardiac defibrillator and deep brain stimulation systems, e.g. employed in treatment of Parkinson's disease, results to be dramatically shorter, down to 3 years [5].

Furthermore the process of miniaturization of batteries have encountered a limit: traditional batteries rely on redox reactions to produce energy, therefore the initial quantity (mass) of reagents determines their capacity and thus lifetime. This implies that implantable devices, which require a certain amount of power for both background activity and actual functioning and should operate for long periods, need a battery which volume usually constitutes more than half of the total one [4]. The cumbersome dimension of such devices can lead to body rejection after implantation and movement limitation in patients everyday life. Moreover, the size of the device sets limitations to the site of implantation: often the stimulating electrodes are connected to the main device through long leads causing discomfort and issues during the surgeries.

Many energy harvesting methods have been proposed in order to avoid the need to implant bulky non-rechargeable Lithium-based batteries and to overcome the constraints they set, as in [6; 7; 8].

One other major concern affecting neural prostheses is related to their mechanical interaction with physiological tissues. Standard CMOS-based electronics and Silicon electronic devices are rigid and cannot well-interact with the compliant and delicate biological tissues and organs. In this context flexible electronics based on organic materials has been deeply investigated in order to match tissues mechanical properties [9]. As a matter of fact stretchable electronics allows sensors, circuitry and electrodes to conform to the shape of the targeted tissue reducing inflammation and friction to a minimum, see section 2.4.

Although the plethora of existing neural prostheses and IMDs requiring novel power supplies or wireless communication systems, this work is carried out in the context of visual prosthesis and in particular is performed in parallel with the fabrication and optimization of the OpticSELINE, an implantable multielectrode array (MEA) employed for targeted neuromodulation of the optic nerve for sight restoration [1]. Hence, we propose an implantable and flexible organic photovoltaic cells array implemented as a signal transducer and governed by a pulsed LED working in the NIR-IR spectral region in order to be optically transmitted through human skin. The final aim of such technology would then be to replace both the implanted power supply, e.g. a battery, and the implantable pulse generator (IPG), in order to achieve a small-sized and flexible device that should be completed with an external module embedding a digital camera, an image processor and a LED system to drive the photovoltaic matrix selective activation.

2 Background

In the following chapter the background and the motivation for this thesis work will be explained. First, a short insight into physiology of vision, blindness and visual prosthesis is presented in order to understand the framework in which this study has been conducted. In particular optic nerve stimulation will be treated separately in order to introduce the OpticSELINE [1], a self-opening intraneural peripheral interface designed at Laboratory of Neuroengineering (LNE) at EPFL and aiming at stimulating optic nerve fibers for sense of sight restoration. A great attention is paid to the OpticSELINE since the photovoltaic organic cells array designed and fabricated during this work has been conceived, in the first instance, for being integrated with this optic nerve stimulation device. Therefore, many of the choices in terms of design and materials have been taken considering the requirements and restrictions set by the OpticSELINE. Materials and power supplies suitable for neural implants and IMDs are then investigated in order to comprehend the background and the state-of-the-art technologies implemented for neural interfaces and prosthesis. Eventually the principle of operation of organic photovoltaic cells is extensively explained.

2.1 Physiology of vision

Vision is the capability of detecting light patterns and of traducing them into images. The visual system is the part of the central nervous system that provides animals with the ability to process visual information. Through the visual pathway animals are able to detect and interpret visible light patterns to build a representation of the outer environment. The visual pathway starts in the eyes and proceeds up to the visual cortex through the optic nerve. The visual signal is processed at multiple levels throughout this path.
The cornea is the first transparent layer encountered by light that enters the eye. The cornea and the crystalline lens are suitable for focusing the image on the retina, where the transduction of light to a nervous signal takes place. The lens is not static, but it is operated by muscles and it can focus and re-focus light on the retina with respect to the distance of the objects in the visual field. In other words, the thickness of the lens is modified in order to tune the focal length. The iris, placed between the cornea and the lens, is a ring-shaped muscle that modulates the quantity of light allowed to enter the eye with respect to the illumination conditions of the surroundings. As above mentioned, the transduction of light into neural impulses occurs at the level of the retina which is located at the back of the eye, as shown in figure 2.1. The retina is a tissue layer composed as follows: the retinal pigment epithelium (RPE), a photoreceptor layer, an inner nuclear layer (INL) and a ganglion cells layer, see figure 2.2.

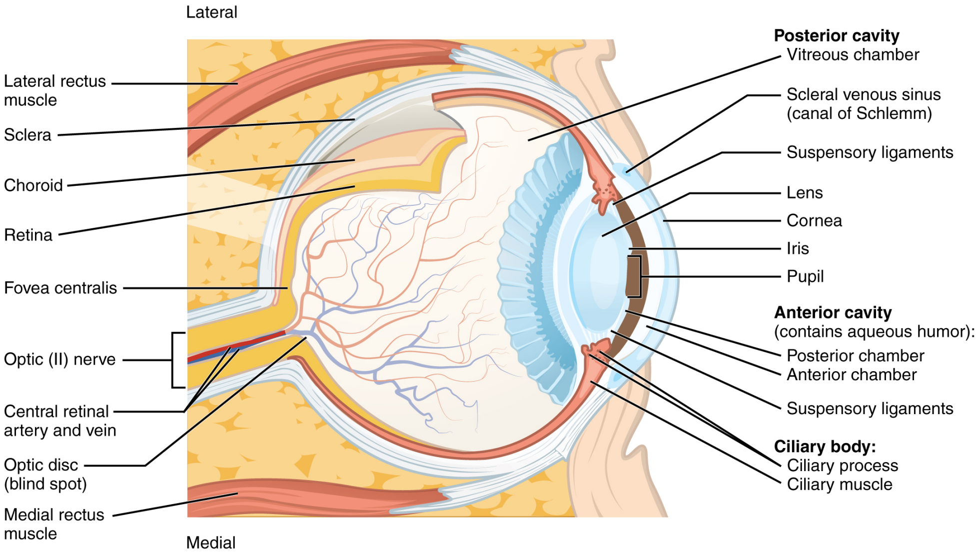

Figure 2.1: Anatomy of human eye, taken from [10]

The photoreceptor layer counts two different types of photoreceptor cells: rods and cones. Both rods and cones are capable of traducing a light pulse in a nervous electrical signal, namely phototransduction process. Apart from their difference in appearance (see schematics 2.2), these cells possess specific characteristics and light sensitivities. Specifically, rods are strongly sensitive to light and thus they are implemented for vision in dim light conditions, while cones, being less photosensitive, are usually used for daytime vision and color differentiation [11]. Both rods and cones contain photopigments, rhodopsin and opsins respectively. Opsins are differentiated into three subtypes, each of which is sensitive to a specific wavelength (blue, green, red). Light impinging on the retina leads to an alteration in photopigments shape starting a cascade of events which ultimately ends with a change in the activity of the retinal ganglion cells. RPE is necessary in order to provide nutrients to the photoreceptors and to allow waste exchange. A large degree of processing of the visual signal is already carried out at the level of the INL. The cells in the INL form synapses with the RGCs which are the ones to generate action potentials.

Interestingly, the optic nerve is constituted by the myelinated axons of RGCs conveying together at the back of the eye. Every fiber carries a specific information such as shape, color, brightness, movement [11]. Some of these fibers directly projects into the back of the brain, while some others constitute the optic chiasm, this crossing to the other side of the brain is useful for coordinating information coming from both eyes. Visual information then reaches the lateral geniculate and from here is transmitted to the primary visual cortex. Ultimately, in the visual cortex specialized cell groups are able to map the visual information and to reconstruct the original image.

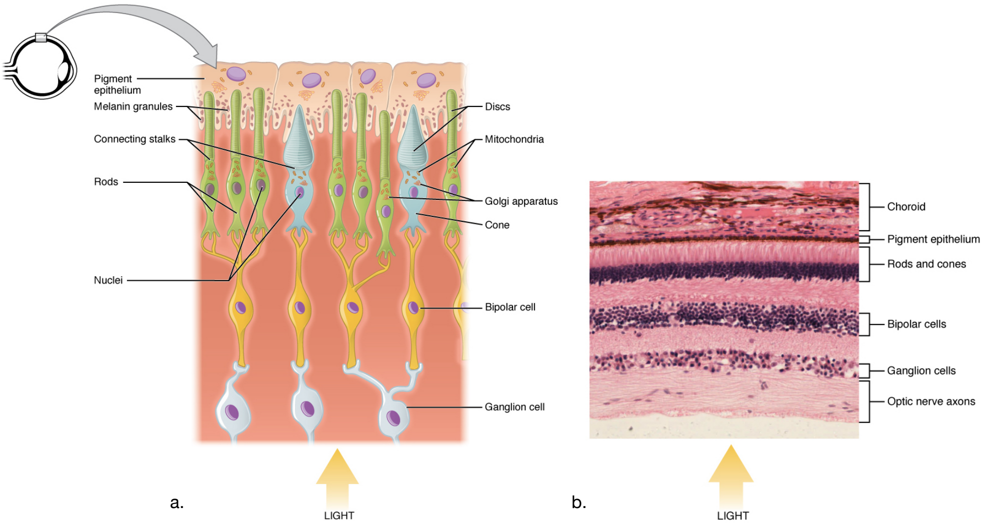

Figure 2.2: Anatomy of human retina, taken and readapted from [10]. **a** Schematics of human retina anatomy. **b** Histological image of human retina.

2.2 Blindness, electrical stimulation of neural tissue and visual prosthesis

A damage at one level of the complex human visual pathway can occur so that the visual information, or part of it, is lost and images of the external environment cannot be reconstructed properly. This condition, usually referred to as visual impairment, can range from a common decreased ability to see to total blindness. In order to establish whether a visual impairment is to be considered as complete blindness two major parameters need to be taken into account: visual acuity, that is the spatial resolution capability, and visual field, that is the area that can be seen when the eye is directed forward, including peripheral vision. World Health Organization has defined thresholds determining the conditions for legal blindness [12]. Globally, 216.6 million people live with moderate to severe visual impairment and 36 million people are estimated to be legally blind [13]. Moreover, population growth and ageing are contributory causes to the continuous increasing of visual impairments worldwide. Vision loss can have a strong impact on quality of life causing inequalities and barriers mostly related to education and employment. Although around 80% of vision impairment conditions can nowadays be treated, a number of diseases still cause vision loss with no possibility to be prevented or cured: it is the case for Retinis Pigmentosa (RP) and Age-related Macular Degeneration (AMD). Both RP and AMD are caused by a gradual degeneration of the photoreceptor cells, rods and cones. Although the interruption of the visual signal flow induced by loss of photoreceptors, the other parts composing the visual pathway which are not affected by these diseases could properly transfer and process an electrical signal. Therefore, if neurons downstream in the visual pathway were electrically stimulated it could be possible to elicit visual percepts in blind subjects. The main goal of visual prosthesis is to exploit nerve cells nature of being electrically excitable and act on the functioning sections of the visual pathway to generate sensations of light, namely phophenes.

From visual impairment to visual prosthesis As mentioned, the visual pathway is long and complex and could get damaged by a disease or trauma at every level, starting from the eye bulb down to the visual cortex. Once assessed the areas affected by the impairment, downstream in the visual circuitry a large variety of locations could be considered potential candidates as stimulation sites. As a consequence visual prosthesis are classified by the location of the stimulating electrodes: retinal, optic nerve and visual cortex (V1) devices, comprising also Lateral Geniculate Nucleus (LGN) [2]. Nowadays, retinal approaches are the most mature in terms of technology and clinical trial so that some retinal prosthetic devices have already been implanted in humans. This is the case for Argus II, an epiretinal device composed of an electrode array positioned on the inner surface of the retina and an external camera to collect visual information from the outer environment [14]. Several reasons have driven researchers to focus on the retina: in first place it allows easy surgical access, moreover it ensures a higher level of physiological processing of the visual signal. The implantation site does not only define the kind of pathologies that can be addressed, but it also sets challenges and constraints due, for example, to easiness of surgery procedures or foreign body reaction after implantation. So, for instance, retinal prosthesis would not be useful if the damage was affecting deeper parts of the visual circuitry, while, on the contrary, LGN devices could help restoring some kind of visual perception. On the other hand visual cortex and LGN devices require extensively invasive surgery procedures and difficulties in the positioning of the probes, while retina and optic nerve are more accessible sites.

Optic nerve stimulation and prosthesis The optic nerve has been addressed as stimulation site as it offers several advantages: first of all it guarantees an easier implantation procedure with respect to other sites further in the visual circuitry. Secondly, an optic nerve stimulation system would allow to restore sight in patients with total retinal impairment or trauma-related visual loss, when it is not possible anymore to exploit the stimulation of residual retinal living cells. Moreover, being a bundle of nerve fibers, the optic nerve could provide with the possibility to activate a large portion of the visual field by stimulating a small area. On the other hand, by being so confined in space it sets new challenges such as specificity and focus of stimulation [15]. Optic nerve prosthesis have been conceived in two forms: as cuff electrodes or penetrating electrodes. In the first case the prosthesis is wrapped around a peripheral nerve and the stimulating electrodes are in contact with the outer nerve fibers and do not penetrate the neural tissue. As it is deducible, the inflammatory response and foreign body reaction are minimized leading to an electrically stable and free of medical complications technology. As an example, in [16] Christie et al. were able to demonstrate the reliability of spiral cuff electrodes for use in motor and sensory neuroprosthesis implanted in human volunteers up to 11 years after surgery. Although cuff electrodes could prove to be an excellent solution for peripheral nerve interfacing, they still suffer of several issues related to mechanical stability and inner fibers stimulation/recording, i.e. specificity and resolution. Penetrating electrodes arrays are, on the contrary, highly stable in terms of mechanical properties and could activate or record neural activity in-situ, meaning that the activation of nerve fibers is not mediated by neighbouring cells. The self-opening neural interface (SELINE) proposed and validated in [17] is one example of implementation of penetrating electrodes arrays for peripheral nerves stimulation. The study carried out by Cutrone et al. is, indeed, the starting point for the investigation and optimization of the OpticSELINE at Laboratory of Neuroengineering (LNE) at EPFL. SELINE, as well as OpticSELINE, overcomes the problem of reciprocal movement within the electrodes and the neural tissue by means of two pair of wings capable of keeping the prosthesis in place.

2.3 Self-opening intraneural electrode for optic nerve stimulation (OpticSELINE)

OpticSELINE is a penetrating looped electrode array suitable for selective neuromodulation of optic nerve fibers. It is a polyimide-based device embedding 12 electrodes built in titanium and gold (six per side, area of 0.008 mm^2) and 2 wings per side positioned in the main shaft (active region, blue box in figure 2.3 **a**). The length of the folded device is 33 mm, while its width is 3 mm at maximum. The current design has been sized in accordance with the anatomical constraints set by the size of rabbit's optic nerve. The novelty of the device lays in the presence of the wings that aim at preventing the device from displacing from its first site of implantation and ensuring a reduction of the signal-to-noise ratio. The implantation is carried out through the implementation of a suture needle that leads the device inside the nerve (the metal transversal bars are necessary for positioning the active area correctly). Once inserted, the OpticSELINE is gently pulled back in order to force the wings to open and stabilize the implantation (see figure 2.3 **c**). In [1] Gaillet et. al could prove an extraction force 30 times larger than that needed for a similar intraneural electrode array without wings which is the corroboration of the stabilization capabilities of the 3D geometry. Moreover, experiments conducted on rabbit's optic nerves strengthened the hypothesis that OpticSELINE could activate the visual cortex in a repeatable and spatially organized manner.

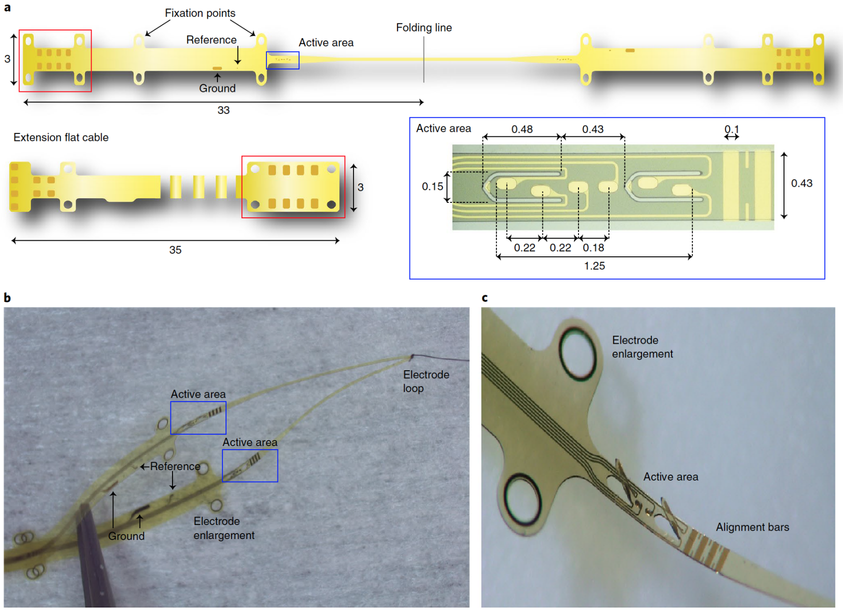

Figure 2.3: The intraneural electrode array OpticSELINE: taken and readapted from [1]. **a** Schematics of the OpticSELINE (dimensions in mm). In the blue box a close up of the active area with 6 electrodes and 2 wings is reported. **b** Photograph depicting a folded OpticSELINE. Blue boxes highlight the active areas. **c** View of the active area with open wings.

2.4 Flexible materials for compliant neuroprosthesis

IMDs and neuroprostheses are devices suitable for restoring physiological functions in people affected by chronic diseases or neurological deficits. Due to their application, these systems must interact and communicate with living tissue at least in an unidirectional way by means of an ionic or electronic flow. We can deduce that the mechanical properties of the implant are a critical feature. Despite its well-established production processes, traditional silicon-based electronics should be avoided in order not to damage soft tissues, e.g. during insertion of the prosthesis, but also to prevent from both acute and chronic inflammation due to the implant-related trauma and the continuous friction between the biological tissue and the sharp synthetic system, respectively. Furthermore, it has been observed how the perpetual inflammation and the scarification due to the contact with inorganic hard materials also degrades the electrical properties of the interface, for instance they cause impedance fluctuations of the electrodes. As a consequence the realization of flexible and compliant devices is a prerequisite for a successful mechanical and electrical interface between synthetic prostheses and human body.
Lacour et al. [18] identify three main parameters to be taken into consideration when designing a neuroprosthetic system:

- the compliance of the targeted tissue
- the size of the implant
- the mechanical contrast between the tissue and the device

The first requires to estimate the stiffness of the tissue that the prosthesis wants to address in order to mimic its mechanical properties. The implant should be as similar as possible to the biological tissue in order to blend in. The size of the actual implant is fundamental for the comfort of the patient, but also for matching the constraints set by the implantation site and the surgery needs. The last requirement deals with the mechanical coupling between the device and the biological sample, the device should be able to bend, expand and torque as the tissue is moving while not altering tissue's natural motion.

In the framework of compliant neural interfaces, PDMS and PI are, so far, the most common materials. Referring to the values reported in table 2.1, PI shows a Young's modulus of 2500 MPa [19], while PDMS only 600 MPa [20] on average. The Young's modulus gives information on how a material behaves when subjected to tensile stress. Having a large Young's modulus implies that the material responds to a given stress with a small strain. Therefore, we can deduce that PI and PDMS will behave differently when the same stress is applied. In particular PDMS will elongate more easily than PI, in their respective elastic regions. Obviously, it is desirable for a neural interface to have lower Young's modulus in order to match tissues behavior. As an example, optic nerve was evaluated to have a Young's modulus ranging from few MPa to few tens of MPa. On the other hand, PI shows a higher tensile strength with respect to PDMS which means that PI handling is easier than PDMS, especially during surgeries. However, both of them presents challenges in the microfabrication processes, in particular when dealing with encapsulation layers. Novel materials, such as Off-Stoichiometric-Thiol-ene Epoxy polymers (OSTE+) firstly developed by Carlborg et al. [21], could be proposed in order to substitute state-of-the-art polymeric films and to overcome the limitations they set. Even though OSTE+ polymers have been mainly proposed for microfluidic and lab-on-chip applications, they can be highly promising for implantable neural interfaces due to their good compliance, low permeability to gases and UV photo-patternability.

For these reasons, OSTEMER^{TM} 322 Crystal Clear (OSTE+ CC) and OSTEMER$^{®}$ 324 Flex

(OSTE+ flex) have been selected as substrate and encapsulation materials for further studies on OpticSELINE devices. As a consequence, due to the strong relation between the present study and the optimization of OpticSELINE, OSTE+ CC and OSTE+ flex are chosen in turn as substrate and encapsulation materials of the device proposed in the following work.

PI	Young's modulus	2500 kPa
	Poisson's ratio	0.34
	Fracture strength	231 MPa
	Dielectric constant	3.4
PDMS	Young's modulus	360-870 kPa
	Poisson's ratio	0.5
	Fracture strength	2.24 MPa
	Dielectric constant	2.3-2.8

Table 2.1: Common materials used for fabrication of neural interfaces: properties. All the values have been taken and readapted from [19] and [20].

2.5 Energy scavenging technologies for implantable devices

As mentioned above, the stiffness and the size of the implant are crucial issues in designing active implantable devices. However, when dealing with chronic implantation the power supply of the device could be as important as the device itself because it requires to be implanted together with the device. In the study of possible solutions for powering minimally-invasive implantable devices, it is of paramount importance to:

- Reduce the total size of the implant;
- Look for possible flexible solutions to be integrated with the flexible device.

Many approaches to deal with this requirements could be adopted: first, one can think to scavenge and harvest energy inside and from the body, exploiting the power which is naturally generated by human body. According to Connor et al. [9] it accounts for roughly 7W of power at rest by considering heat generation, breath and blood pressure. For instance, one could think to scavenge kinetic energy from body or organs motion and traduce it into re-usable electrical energy for powering IMDs or biosensors. This goal could be achieved, for instance, through the implementation of piezoelectric energy harvesters that, indeed, convert mechanical stress into an electrical signal. Indeed, several flexible piezoelectric energy harvesters have already been produced and validated, as in [22; 23]. Other solutions that have been proposed rely on electromagnetic and electrostatic harvesters. Such devices can generate an electromotive force in response to a modification of an external magnetic flux through a closed circuit [24]. Unfortunately, this approach can hardly be integrated with a flexible IMD. All the presented solutions can help to reduce the size of the implants by getting rid of cumbersome batteries, but even though smaller, they still relies on the presence of an accumulator. Moreover it is not always possible to scavenge power in-situ because of the lack of reliable energy sources, it is the case for visual prosthesis. As a consequence leads would be necessary to connect the energy scavenging system and the device, causing discomfort and medical complications. In alternative to the above mentioned approaches, researchers have studied solutions to transfer energy wirelessly from the outside to the inside of the body. Inductive links, for

example, could be used to power implantable devices. Again, the problem with this kind of technology is the difficulty to fabricate flexible alternatives. The photovoltaic solution has also been considered as a attractive candidate by many research groups. As a matter of fact a large percentage of the solar spectrum can penetrate skin, making it possible to scavenge energy from implanted photovoltaic systems. According to the application, it is possible to decide whether to implement an inorganic, hybrid or organic approach.
In [25], Ayazian et al. propose a silicon based and CMOS compatible P+/N-well photodiode array for powering implantable sensors, while Moon et al. in [26] could demonstrate a high power conversion efficiency for both Si and GaAs photovoltaic solutions implanted in mice. Interestingly, both hybrid and organic solution can be easily conceived in a flexible alternative. Research upon flexible/stretchable optoelectronic devices is quite mature thanks to the several possible applications they can serve, not only in the biomedical field.
Concerning flexible photovoltaic cells, many researchers adopted an hybrid organic-inorganic solution by embedding inorganic solar cells array in a polymeric stretchable encapsulation. The minimal thickness of the metallic/semiconductor layers together with the implementation of strategies to achieve stretchable interconnects, as in [27; 28], have made possible to fabricate highly efficient photovoltaic devices based on the well established p-n junction configuration on flexible substrates. To cite one example, Song et al. obtained a PCE of 21.5% for a GaAs cell on a flexible polyimide substrate [29]. A totally different approach is to entirely build the cell with organic materials. Kaltenbrunner et al. were able to build a totally organic solar cell based on P3HT:PCBM on PET [30]. One other successful implementation of organic solar cells is, for instance, presented in [3]. Interestingly, Ferlauto et al. exploited organic photovoltaic pixel based on P3HT:PCBM in order to generate pulses to stimulate retinal cells to restore vision in blind patients. The novelty of the proposed device lays in the fact that no battery, neither an IPG should be implanted, since the device acts as a transducer from light power into electrical power. The study we propose hereunder is based on this idea, i.e. exploit an organic and flexible photovoltaic cells array in order to substitute, and not to power, an implantable pulse generator (IPG). As a matter of fact by implanting a matrix of photovoltaic cells governed by an external module, not only there would be no need for implantable batteries, but also IPG and accumulators could be avoided.

2.6 Organic photovoltaic devices

The major difference existing between inorganic and organic solar cells is the nature of the photon-to-electron conversion region of the device: those photovoltaic devices showing an organic semiconductor material as photo-active layer are, indeed, considered organic solar cells. Organic semiconductors are carbon-based materials showing semiconductive properties which are the result of the nature of bondings between carbon atoms. In conjugated polymers the σ bonds forming the backbone are alternately single or double. This means that three of the four carbon's valence electrons are employed in σ bondings, while one is left in the p_z orbital. The overlap of electron wavefunction of neighboring atoms along the backbone of the polymer allow the delocalization of π carriers, hence these electrons do not belong to a single atom in the chain, but rather to all "connected" atoms. This results into an energy bands-like structure where it is possible to define a bandgap and the HOMO (highest occupied molecular orbital) and LUMO (lowest unoccupied molecular orbital) energy levels [31]. From a macroscopic standpoint, it is possible to study the band structure of organic materials in a similar way to the band structure of inorganic materials. Similarly to the valence band, the LUMO state is normally filled with electrons while the HOMO state is the analogue of the conduction band and is generally free of electrons [32]. Organic semiconductor materials have become appealing for optoelectronics application due to their capability, similarly to inorganic materials, to absorb photons allowing a transition from a ground state to an excited state. The only difference lays in the fact that when an electron is excited from HOMO to LUMO, the molecule itself owns the energy of an excited energy state and not only the free electron in the conduction band [32].

2.6.1 Principle of operation

Similarly to inorganic solar cells, an electron-hole pair is generated if a photon carrying enough energy impinges on the photo-active material/layer of the solar cell and it is absorbed. The absorption of light in organic materials induces the generation of localized excited states or bound excitons. The carriers which constitute the excitons are not instantaneously free (non-Coulombically bound) and their spontaneous separation is highly improbable, so they need to be separated by a driving force. Usually two different metallic conductors with different highest occupied energy levels are employed as electrodes. In this framework, the electrons are forced to flow from the conductor with the highest energy electrons to that with the lowest energy electrons until the point when they reach the same chemical potential. This motion of charges sets up an electric field across the organic material which provides indeed the energy for exciton separation.
Organic solar cells can be built as single layer, bi-layer or bulk heterojunction. The first one consists of one layer of organic semiconductor deposited in between two electrodes built with materials showing different workfunction in order to enhance charge separation (Figure 2.4 **a**.). Acceptor-donor interface technology has been introduced to overcome the extremely low efficiency of single layer solar cells ($< 1\%$) by placing in contact a film of a donor material with a film of an acceptor material, the first being characterized by a high LUMO, the latter by a low HOMO. This solution enhances the performances of the solar cells by facilitating the operation of separation of the generated exciton. Both bi-layer and bulk heterojunction solar cells are based on this principle, the structure of the two types of cells is shown in figure 2.4 **b** and 2.4 **c**. Considering the high efficiency characterizing BHJ solar cells, our experimental work had been totally based on this type of cells. From this point the attention will be focused on BHJ photovoltaic cells.

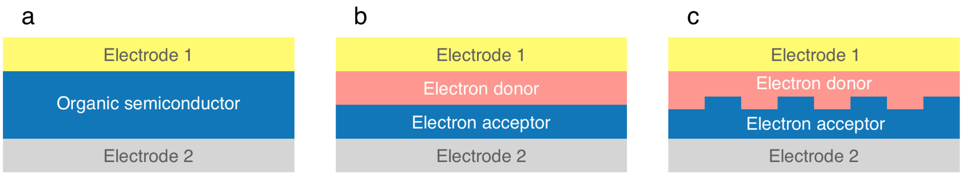

Figure 2.4: Structures of organic solar cells: **a** Single layer **b** Bi-layer **c** Bulk heterojunction

Optical Absorption and Exciton Formation

We have previously stated that from a macroscopic standpoint an organic semiconductor material can be studied in a similar way to an inorganic semiconductor, defining a LUMO and a HOMO in the same way as we can recognize the conduction band and the valence band of an inorganic material, respectively. Therefore, an energy band gap E_g can be defined as the difference between the HOMO and the LUMO energy levels. When a photon collides on the absorber molecule it can either be transmitted or absorbed. The probability that one or the other process occur depends upon the wavelength, and thus the energy, of the impinging photon: if the incoming photon carries an energy which is smaller than the energy band gap, it will be transmitted as it cannot cause a electron transition in the material. However if its energy is equal or greater than E_g, then it is highly probable that it will be absorbed and it will induce a transition of one valence electron from the ground state to an excited state, generating a Coulomb-correlated electron-hole pair, namely exciton. The absorption process can be described through the absorption coefficient of the photo-active material $\alpha(\lambda)$ which gives information on how far a beam of incoming photons with a specific wavelength can travel through the material before being absorbed. The process follows the well-known Lambert-Beer law:

$$I = I_0 \cdot e^{-\alpha x} \tag{2.1}$$

With I being the intensity of the beam at the position x in the material with absorption coefficient α and I_0 the initial intensity. We can deduce that the intensity of the beam is decaying exponentially with a velocity that depends upon the absorption coefficient. It is of paramount importance in the design process of both organic and inorganic solar cells to take this phenomenon into account in order to tune the thickness of the active layers so that the greatest fraction of the beam is absorbed in the photo-active area.

Exciton Diffusion and dissociation at the Donor - Acceptor Interface

In an organic semiconductor material, the electron-hole pair which is generated due to the absorption of a photon is not a couple of free carriers, instead it is constituted by Coulombically bound carriers, or exciton, which, for instance, could show binding energies of 0.7 eV (much higher than that of inorganic semiconductors that is of the order of few meV) [33]. This means that carriers cannot be immediately collected, but first they need to be separated. One of the most common strategies to achieve successful charge separation is to integrate an electron donor (rich of electrons) and an electron acceptor (poor of electrons) in the photosensitive layer. One requirement to obtain an efficient exciton dissociation is to exploit materials showing an offset in the energies of the LUMOs. This potential difference is then the driving force that enables electrons to move towards the lower energy level (acceptor's LUMO) as free carriers. It is worth to mention that the average diffusion length of free electrons in an organic semiconductor material is approximately 10 nm. However, as mentioned before, the absorption process strongly depends upon the active layer thickness. In order to collect a large portion of the incoming photons, but at the same time not to lose many carriers due to recombination a trade-off is needed. Bulk heterojunction solar cells were developed to avoid this kind of issue because they rely on a blend of a donor material and an acceptor material which are deposited together and form a complex network (see figure 2.5 **a**) were electrons can diffuse easily and fast from one phase to the other.

2.7 Purpose of the study

In the present work we propose the idea of a novel wireless implantable pulse generator for targeted neuromodulation of the optic nerve based on organic photovoltaic cells. The aim is to substitute cumbersome implanted batteries and IPGs in order to pave the way for a flexible and mini-invasive device. The compliance of the system is to be ensured by the implementation of polymeric materials both for the substrate and for the photo-active film of the cells. The prototypes we present in the following study consist

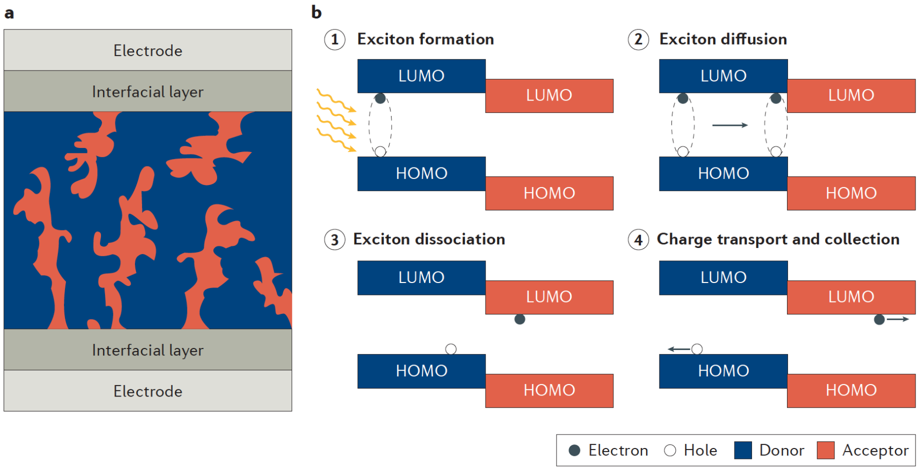

Figure 2.5: a General structure of a bulk heterojunction solar cell. The representation of the photo-active layer (blue and red) aims at showing how acceptor's phase and donor's phase are interpenetrated when deposited in form of a blend. Due to the mutual interpenetration of materials, the electrons can be collected by the acceptor material before they are recombined. **b** Working principle of a bulk-heterojunction organic solar cell. When a beam of photons impinges on the organic semiconductor (donor material), an exciton is generated. The exciton diffuses to the materials interface and here is dissociated thank to the energy difference between the LUMO levels of the two materials. Once the carriers are separated, they can be collected as free carriers. Taken from [33]

of one organic photovoltaic cell connected to one electrode in local return configuration. Such configuration of electrodes is currently under study at Laboratory of Neuro-engineering (LNE) at EPFL in order to guarantee a highly selective stimulation of nerves fibers with reduced cross-talk with neighbouring electrodes when arranged in a matrix. The organic photovoltaic system will be designed as a bulk heterojunction solar cell, meaning that the photo-active function is served by a blend of an electron donor and an electron acceptor material. The BHJ approach ensures higher efficiencies compared to other organic photovoltaic systems due to the interpenetration of acceptor and donor materials that enables a faster charge separation, within the lifetime of photo-generated carriers inside the materials. Although organic donor materials working in the visible light range have been subject of several studies and are thus the most mature technology, the need to transmit light through the human skin, while limiting the power losses, sets a new challenge to this work. Narrow-band conjugated polymers showing a maximum of solid-state absorption in the NIR-IR range will thus be investigated to serve this purpose. Therefore, the objective of the following study is to research suitable materials and microfabrication procedures enabling their usage.

3 Materials and methods

In the following chapter the design and the materials of the photovoltaic cells and the stimulating electrodes are explained in detail. Subsequently, an overlook about encapsulation and substrate materials choice will be presented. Section 3.2 contains the complete first and last optimized process flow for the fabrication of the devices. The two production processes are extensively analyzed in order to be compared. In particular, the modifications brought during this work to the final prototype will be highlighted both in this chapter and in chapter 4. All the fabricated prototypes have been virtually grouped in four batches: the first comprises the wafers fabricated as in 3.2.1, while the fourth is the last produced prototype following the process flow presented in 3.2.2. The third and the second batches are intermediate prototypes that are shortly presented in section 3.3. The transitions from one prototype to the following and the underlying motivations will be better analyzed in 4 in order to justify the modifications that this study has brought to the device. Eventually, the techniques that have been used to characterize and validate the fabricated devices will be explained. In particular, the attention will be focused on the electrochemical characterization of the electrodes, i.e. impedance spectroscopy (IS) and cyclic voltammetry (CV), and the photovoltaic characterization of the cells.

3.1 Design

The design comprises twelve photovoltaic cells connected to one single electrode in local return configuration (see section 3.1.2), the whole design is depicted in figure 3.1. The electrodes are concentrated in two areas of the wafer in order to facilitate the positioning of pools containing saline solution or Phosphate-buffered saline (PBS) for the electrochemical measurements. The cells were designed in six different diameters: $1000\,\mu m$, $750\,\mu m$, $500\,\mu m$, $300\,\mu m$, $200\,\mu m$ and $100\,\mu m$. The decision to diversify the cells on the wafer aims at verifying which size is more suitable for the application in terms of microfabrication issues and generated photo-voltage and photo-current. The purpose of the measurement pads, i.e. the external circular structures connected to the traces or directly to the cell, is to allow the recordings of electrical signal during the experiments.

3.1.1 Measurement configurations

As it can be observed in figure 3.1, the measurements pads are connected differently for two cells of the same size. A close up of the two configurations is reported in figure 3.2. Figure 3.2 **a** depicts the first and more intuitive type of connection: the measurement

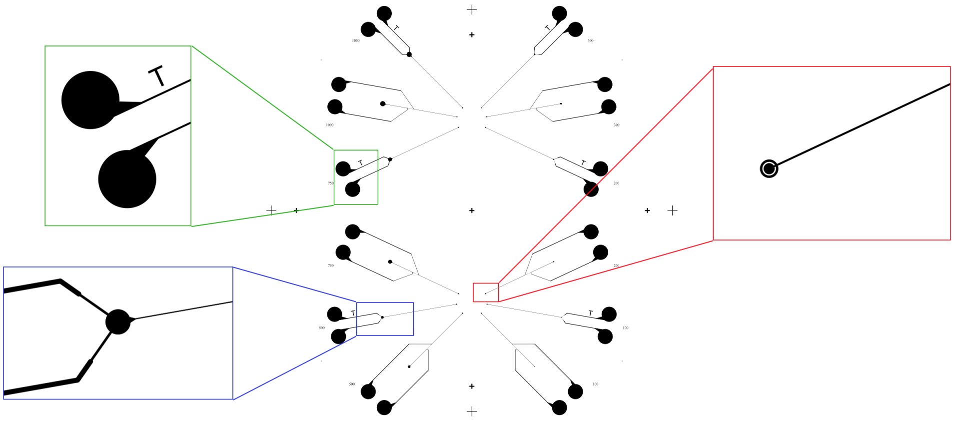

Figure 3.1: Design of the devices for electrochemical and photovoltaic experiments. Each wafer embeds twelve devices, thus twelve electrodes, twelve organic photovoltaic cells (ranging from 1000 µm to 100 µm in diameter) and twenty-four measurement pads. In figure, a close-up of the measurement pads (green), of a photovoltaic cell (blue) and one electrode in local return configuration (red).

pad indicated by **T** in the design, where T stands for "top"[1], is connected to the cathode of the cell, while the other is connected to the anode. Basically, in this first case the traces are prolonged to the pads allowing the current to flow from the electrode to the pad through a low impedance path during the electrochemical characterization. Figure 3.2 **c** depicts the equivalent circuit related to this first configuration. As it can be observed, when there is no illumination and contemporary a voltage is applied to the nodes, the current goes through the low impedance path: the electrode and the electrolytic bath, instead of flowing through the photo-diode. In the second configuration, reported in figure 3.2 **b**, one of the measurement pads is directly connected to the cathode, while the second is only connected to the top conductive layer of the photovoltaic cell. Therefore, if a photo-voltage is generated across the photovoltaic cell, the current will be forced to flow through the electrode and thus through the electrolytic solution, returning a more realistic result which takes into account the metallic conductor-electrolyte interface and the losses that could appear at this step. The equivalent circuit is depicted in figure 3.2 **d**.

3.1.2 Electrodes design

Nowadays, one major issue concerning visual prosthesis is related to the spatial resolution of the stimulation. The spatial resolution has to deal with the density of electrodes, but also with the selectivity of the stimulation, i.e. ideally cross-talk within neighbouring electrodes should be avoided. Generally, implantable devices rely on the presence of their own case as a return "electrode": when the pulse is delivered via the working electrode, the current flows through the neural tissue, modeled with its own conductivity, and closes the circuit on the case [35]. It is easy to deduce that the selectivity in this case is not optimal and that along the current path many non-targeted neurons can fire action potentials. Local return electrodes are under investigation at the Laboratory

---

[1] Taken in consideration the multilayered structure of the device, we have referred to the anode as "bottom" electrode and to the cathode as "top" electrode. The appellatives are due to the materials order of deposition in the microfabrication process.

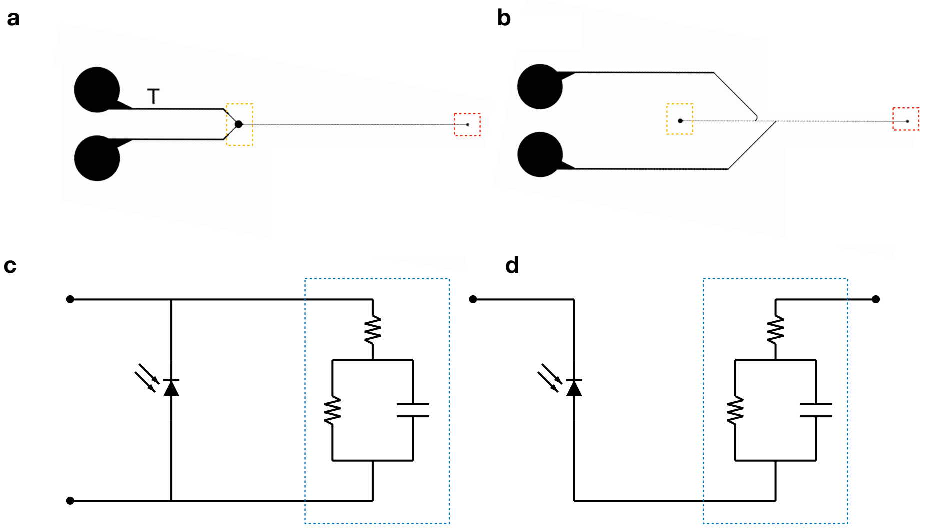

Figure 3.2: **a** First measurement configuration: anode and cathode are directly connected to measurement pads. **b** The cathode is directly connected to a measurement pad, while the anode is connected to a pad indirectly: the circuit is closed through the electrolytic bath. **c** First configuration equivalent circuit. **d** Second configuration equivalent circuit. The blue dashed box highlights the electrode model: a resistance, mimicking the connection lines, in series with a parallel of one resistance and one capacitance standing for the electrode/electrolyte interface. The equivalent circuit model for electrodes has been taken from [34].

of Neuroengineering (LNE) in order to overcome this limitation and to improve the selectivity of stimulation, towards single neuron stimulation. Other research groups are studying local return effectiveness, to cite one Palanker et al. at Standford university are simulating and producing retinal prosthesis with high selective stimulating pixels in local return configuration [36]. At LNE, local return electrodes have been optimized with respect to stimulation specificity and electrode size. The design trade-offs have led to the optimal shape and size depicted in figure 3.3. The design we propose include local return electrodes as in figure 3.3. The ring-shaped return electrode is designed to match the area of the cathode: the total exposed area of the cathode is 10 207 µm, while for the anode is 10 112 µm. Although, in the original design of local return electrodes the cathode was at a lower level with respect to the anode, in our design the electrodes have been inverted. Being generated by a photovoltaic cell, the stimulation pulse cannot be driven to the desired electrode; this configuration assures that the cathodic current, which was proven to be the most effective in terms of stimulation [35], is delivered through the central electrode and recollected through the annular anode.

Together with spatial resolution one other major parameter affecting stimulation is the charge storage capacity (CSC). CSC is defined as the total amount of charge per unit geometric surface area available for one electrode. It has become common practice to use the chatodal charge storage capacity as a comparative measure between stimulating electrodes. Electrodes made of noble metals have been widely employed for stimulation because of their durability. However, with the current trend in reducing electrodes size in favour of selectivity and mini-invasive implants, noble metals show insufficient charges storage capacities. As a consequence, novel materials are being investigated. In particular the attention is focused on porous or nanostructured alternatives that increase electrodes electrochemical surface area. For the above mentioned reasons, in this work the electrodes will be coated with a sputtered iridium oxide film (SIROF) in order to improve the CSC.

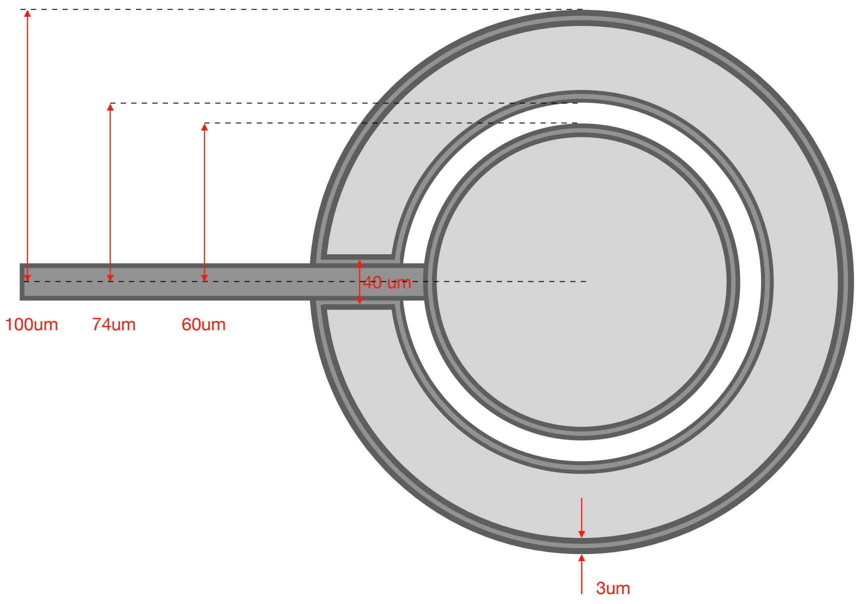

Figure 3.3: Local return electrodes design. The external ring represents the return electrode, while the central circle the stimulating electrode. This novel design bringing the return electrode close to the stimulating electrode enhances the selectivity of the stimulation by focusing the electric field. The active areas of the cathode and the anode have been sized to be similar in order to ensure charge balance. The shape and size of local return electrodes have been studied and optimized at the EPFL Laboratory of Neuroengineering (LNE).

3.1.3 Photovoltaic cells design

Due to their high efficiency and easiness of blend preparation, the photovoltaic cells have been designed as fullerene based bulk heterojunction organic solar cells.
The first layer of the materials stack is an anode built in Indium Tin Oxide, or ITO (purple in figure 3.4). ITO is a material constituted by three basic elements: indium, tin and oxygen in tunable proportions. Depending upon the percentage of oxygen contained in the composition it can either behave as a ceramic or a metal. When deposited in thin films, for instance through evaporation or sputtering, it is transparent to a wide range of the visible spectrum which is one of the reasons why it has been extensively implemented as a transparent electrode. It can reach very low sheet resistances according to the ratio between the elements and the thickness of the deposited film. However, while increasing the thickness the transparency is partially lost. In particular in the case of a photovoltaic

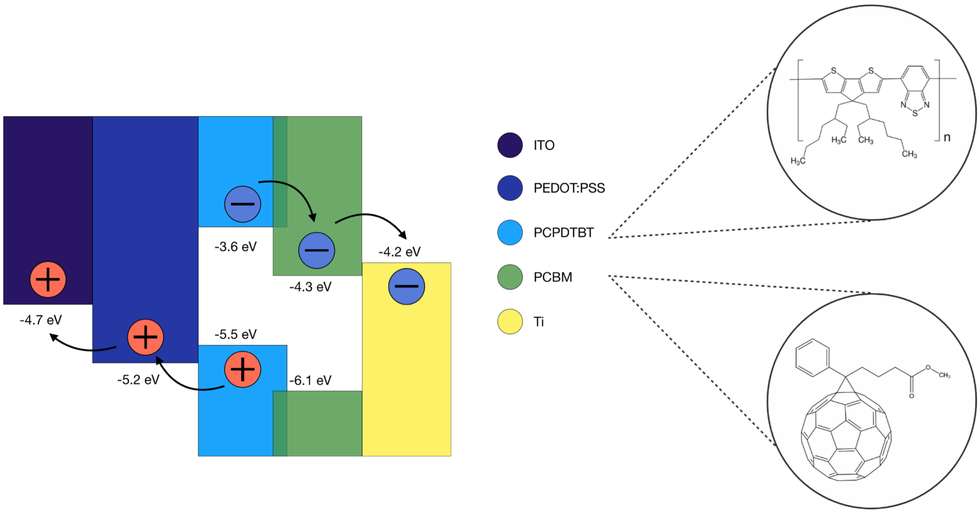

Figure 3.4: Schematics of photo-active materials stack band-diagram. The workfunction of inorganic materials as well as the HOMO and LUMO levels of organic materials are depicted with respect to the vacuum level. The arrows show the progression of charge carriers from generation to dissociation.

cell the transparency of at least one of the electrodes is a necessary condition. Temperature of operation is probably the most critical parameter to be set: ITO can be deposited either at room temperature or at very high temperatures, the result in terms of sheet resistance is strongly variable. In addition, a greater attention should be paid when dealing with flexible and organic electronic devices because of the strong sensitivity of polymers to high temperatures.

The second layer is constituted by a film of PEDOT:PSS doped with 0.1% of GOPS (blue in figure 3.4). Poly(3,4-ethylenedioxythiophene) polystyrene sulfonate, or PEDOT:PSS, is a polymer mixture composed of two ionomers, a sulfonated polystyrene (PSS), bringing a negative charge, and a conjugated polymer (PEDOT), bringing a positive charge. Ionomers are polymers which backbone is covalently bonded with two varieties of pendant groups: an electrically neutral unit and an ionized one. The classification of a polymeric material as an ionomer depends upon the level of substitution of the ionic groups. Remarkably, PEDOT is a conjugated polymer and thus conductive. As previously mentioned a conjugated polymer has delocalized π electrons belonging to all connected atoms through overlapping of p orbitals. As an effect of delocalization of π electrons PEDOT results as conductive and stable. Due to its intrinsic electrical conductivity, its optical properties and its versatility in terms of fabrication techniques, PEDOT:PSS has become one of the most exploited conductive polymers. PEDOT:PSS is a p-type semiconductor and it is optically transparent in the visible light range, therefore it is suitable as a transparent electrode in optical applications such as organic solar cells or organic LEDs [37]. Although its solubility in water is a desirable feature during deposition steps, it could be a deceptive property when dealing with applications in aqueous environments. In order to avoid delamination of the film or degradation of its properties (3- glycidyloxypropyl)trimethoxysilane (GOPS) has been implemented to cross-link PEDOT:PSS. It has been proven that GOPS stabilizes PEDOT:PSS while just slightly worsening its electrical conductivity and light absorbance [38]. To summarize, PEDOT:PSS has been chosen as a buffer layer because of its intrinsic high work-function and thus good holes conductivity and it has been doped with GOPS in order to confer with stability in water environments.

The photosensitive blend, schematized in figure 3.4 as light blue and green overlapping bands, is the core of a bulk heterojunction photovoltaic cell. The open-circuit voltage (V_{oc}) and the external quantum efficiency (EQE) all depend upon the choice of the materials composing the blend [39]. As mentioned before, the photo-active layer is based on an acceptor-donor blend because of the requirement of ultrafast charge transfer at the interface. Many research groups reported high efficient solar cells based on P3HT as donor material, a conjugated polymer showing a bandgap of 1.9 eV and absorption maxima ranging between 400 and 650 nm [40]. However, for an implantable device it could be interesting to use a narrow bandgap conjugated polymer in order to shift the maximum of absorption towards infrared and thus reduce losses due to skin absorption. For this reason we have focused on PCPDTBT, a narrow band conjugated polymer with a maximum of solid-state absorption approximately on 770 nm. On the other hand, $PC_{60}BM$ is one of the most common choices for an acceptor material. $PC_{60}BM$ is the abbreviation for fullerene derivative of C60 buckyball, [6,6]-phenyl-C61-butyric acid methyl ester. It is very practical in the context of fabrication of BHJ photovoltaic cells because it is soluble in chlorobenzene as PCPDTBT and P3HT are. This feature allows to mix together acceptor and donor solutions to constitute and deposit the blend.

The last layer, i.e. the cathode, is built in titanium (yellow in figure 3.4). The choice of Ti as the cathode material is mainly due to its work function capable of creating an ohmic contact with PCPDTBT:PCBM for electrons scavenging.

3.1.4 Substrate and encapsulation materials

It is well-known how important it is for an implantable medical device to be compliant and to merge with the biological tissue in order to avoid chronic inflammation, formation of the fibrotic capsule and deterioration of the electrical properties [18]. As a consequence substrate and encapsulation materials choice become crucial in the design of the devices. Polyimide and PDMS have been extensively investigated in many state-of-the-art studies as both substrate and encapsulation materials, as mentioned in 2.4. However, they both present some drawbacks. For example, PDMS and PI are normally non-photo-patternable which means that encapsulation substrates need to be etched in order to open the electrodes and the electrical connections. Moreover, PI in particular shows a relatively high Young's modulus that can cause a mismatch with the host tissue. In this framework, the decision to create a new generation of OpticSELINE devices based on OSTE+ polymers has been taken.

OSTE+ polymers: fundamental properties description OSTE+ are photo-patternable polymers based on off-stoichiometric thiol-ene epoxies. The curing procedure is performed in two sequential steps. First the radical photo-polymerization, carried out via UV illumination at 375 nm, which consists in the reaction between -SH thiol groups and -ene groups. This first reaction triggered by UV illumination allows to pattern OSTE+ layers, for instance spin-coated on a wafer, by selectively exposing the films. The non-polymerized portions can thus be removed. Subsequently, a thermal anionic polymerization consisting in epoxy groups reacting with residual thiol groups in order to form an inert polymer can be triggered by means of a thermal curing [41]. OSTE+ polymers purchased from Mercene Labs are delivered in 2 components, A and B, the first containing the thiol group, the second containing the allyl group, the epoxy group, the photo-

initiator and the base catalyst.
We have implemented two types of OSTE+ polymers:

1. OSTEMER 322 Crystal Clear (OSTE+ CC) - A:B ratio of 1.09:1;

2. OSTEMER 324 Flex (OSTE+ Flex) - A:B ratio of 1.24:1.

Preliminary studies carried out at LNE – EPFL by Borda E. helped to determine the fundamental mechanical properties of both OSTE+ CC and OSTE+ flex. In particular, Dynamical Mechanical Thermal Analysis (DMTA) has tested how OSTE+ CC and OSTE+ flex Young's modulus (E) behave with respect to temperature variations. The results showed that at physiological temperature OSTE+ CC Young's modulus is approximately 2.5 GPa, while OSTE+ flex Young's modulus is 30 MPa.
One other key feature of OSTE+ polymers for OPV applications is their optical transparency to most of the visible, NIR and IR spectrum, that allows optical transmission through the substrate and encapsulation layers without great power losses.
For all these reasons, one of the final aims of this project was to pave the way for a totally OSTE+ polymers-based device. As a consequence the following discussion about microfabrication will be focused on acting the transition from traditional flexible polymers to OSTE+.

3.2 Microfabrication

All the prototypes have been fabricated and characterized within Campus Biotech, in Geneva, and CMi (Center of Micronanotechnology) at EPFL, in Lausanne. Below, the first and the final process flow are described and the main choices in terms of microfabrication are justified. For sake of completeness, it is important to mention that the first batch of wafers was produced with a slightly different design. Indeed, the main layout was the same as for all the following wafers with a difference in the size of the photovoltaic cells: the cells fabricated during the first set of experiments were 2.5 mm in diameter, however arranged with the same ratio on the wafer.

3.2.1 First prototype process flow

Surface cleaning and activation The fabrication takes place on a 4 inches glass wafer. First the surface of the wafer is cleaned and activated through an oxygen plasma. Plasma is rich with highly reactive chemical species, therefore it can help to start a variety of physical and chemical processes upon contact with the wafer substrate, in this case glass. Within this multitude of processes it is worth to mention:

- ultra-fine cleaning, i.e. conversion of contaminants into volatile species such as carbon dioxide and water and their subsequent elimination by evaporation;

- Promotion of three-dimensional cross bonding of molecules and bonds breaking by means of oxygen radicals;

- Metal-oxides and hydrogen species reaction resulting in superficial metal-oxides reduction to metal atoms and water;

- Deposition of short-lived functional chemical species, such as polar OH, that increase surface energy and wettability.

Adhesion promoter layer deposition After surface activation, VM652 adhesion promoter is spin-coated on the wafer and let to dry. Although the final devices would be supposed to be released from the wafer, these samples where produced to optimize the process flow and to perform experiments, therefore they are not required to be released.

PI substrate spin-coating After VM652 drying, a 10 µm substrate layer of Polyimide (PI2611) is deposited via spin-coating (figure 3.5**1**). PI2611 requires a triple set of bakings after deposition to be cured, therefore it is first subjected to a first 5 minutes soft bake at 65 °C, then to a 5 minutes soft bake at 95 °C and eventually it is loaded in oven for an overnight hard bake program ramping up to 300 °C. Spin-coating has been chosen for polymers deposition because of the good uniformity and repeatability of wet films that it can produce. This technique is particularly interesting because of the easiness of thickness tuning by setting the speed of rotation of the plate. Furthermore a wider range of thicknesses (from 1 nm to µm) can be reached compared, for instance, to doctor blade deposited films. Spin-coating is a common choice for small substrates and batch processing, but it is totally unsuitable for industrial large-scale production. In addition it requires to be patterned after deposition which makes it compulsory to adopt further strategies and steps, making the process flow more time-consuming and expensive. In the following work this technique has been adopted for all wet films deposition.

Photolithography - Ti bottom layer It is now important to mention that the first prototypes have been designed to have an ITO layer as bottom electrode, but the bottom traces and the measurement pads built in titanium (see figure 3.5 **A**). As a consequence to this choice, the first photolithographic step is performed in order to define the shapes of the ring-shaped anodes, a ring along the perimeter of the photovoltaic cell's bottom electrode and 6 of the measurement pads dedicated to the configuration **a** of figure 3.2. These structures are patterned onto a 2 µm layer of positive photoresist AZ® 1512 (figure 3.5 **2**). This first photolithographic step is performed exploiting the maskless Aligner MLA150 by Heidelberg Instruments. The maskless photolithography allows a fast and high-resolution exposure without the implementation of a lithographic mask, as the system defines the pattern directly onto the resist-covered surface by means of a laser beam. This means that possible errors or design modifications do not require a new mask fabrication, but a fast CAD layout modification. The maskless technology ensures a resolution limit of 600 nm, therefore in case of need for nanometric features traditional photolithographic systems would be more effective. The smallest feature contained in our design is approximately of 10 µm so that a higher resolution is not required. Once exposed, the photoresist is developed in order to remove the exposed material.

Ti sputtering Using the AC450CT sputtering system by Alliance concept, 200 nm of Ti are sputtered onto the wafer (figure 3.5 **3**). Among all, sputtering is the PVD technique that can reach the highest quality films endowing with the best uniformity and impurity level. What makes the sputtering technique very appealing for the fabrication of organic devices is the operation temperature: deposition can be run at room temperature entailing no damage to polymeric films.

Ti lift-off In order to selectively remove unnecessary material on the wafer a lift-off step is carried out. Photoresist is used as a sacrificial layer: when the wafer is immersed in a solvent the photoresist is washed away and the material on the top is lifted-off. We have performed the lift-off in PGMEA under continuous sonication.

Photolithography - ITO bottom layer A second photolithography is exploited to deposit ITO as a bottom electrode for the photovoltaic cell. Similarly to the first, the pattern is transferred onto a 2 µm layer of AZ® 1512 via the MLA150 system (figure 3.5 **4**).

ITO sputtering and lift-off After patterning and development, 200 nm of ITO are sputtered on the wafer (figure 3.5 **5**). A step of lift-off in PGMEA is used again to remove the unwanted material (figure 3.5 **6**).

PEDOT:PSS and PCPDTBT:PCBM spin coating The following step consists in the spin coating of PEDOT:PSS and PCPDTBT:PCBM and should be performed in inert atmosphere, for this reason the following procedure is carried out in glove-box. Prior to spin-coating the surface is activated with a weak oxygen plasma which helps to improve the wettability of the surface and thus facilitates the solution deposition. 1 mL of PEDOT:PSS with 0.1% GOPS is poured on the wafer and spun to obtain a uniform coating (figure 3.5 **7**). The curing of the polymeric film consists of a 30 minutes baking at 110 °C. The wafer is then let to cool down. Similarly, 35 µL of PCPDTBT:PCBM in chlorobenzene is spin-coated on top of the PEDOT:PSS layer (figure 3.5 **8**). As well as the first polymeric layer, the photo-active film is baked for 30 minutes at 110 °C. Eventually, the wafer should be left in inert atmosphere overnight.

Ti sputtering through shadow mask A shadow mask is now positioned on the wafer and aligned, the apertures are only in correspondence of the photovoltaic cells. The purpose of the mask is to selectively sputter titanium without the need of a photolithographic step and subsequent lift-off which is detrimental for the spin-coated polymers (figure 3.5 **9**).

Polymers etching The sputtered Ti acts as a mask for the polymers etching step and enables to preserve the polymers only on the photovoltaic area. A Reactive Ion Etching (RIE) is carried out implementing the etch system 210IL ICP-RIE by Corial. RIE is a good match with the specifications set by our design and process flow:

- it is directional, so it endows with very small under-etching;
- it is a dry etching technique which means that no solvents or other liquids are brought in contact with the photo-active polymeric layer with the risk to be damaged or washed away.

At this stage the stack composing the photovoltaic cell is complete (figure 3.5**10**).

First encapsulation in OSTE+ Flex A 5 µm layer of OSTE flex is deposited via spin-coating as a first encapsulation layer and it is UV-patterned through the MLA150 system in order to create apertures for the photovoltaic cells, the electrodes bottom section and the measurement pads (figure 3.5 **11**). After development in Ethyl L-Lactate, the polymerization of the encapsulation layer is ended with an overnight bake at 100 °C.

Photolithography - Ti top layer A third photolithographic step performed with MLA150 allows to pattern the shapes of the electrodes top layer and measurement pads into a 2 µm layer of AZ® 1512 photoresist (figure 3.5 **12**).

Ti sputtering and lift-off Titanium is deposited through sputtering (figure 3.5 **13**) and a lift-off process in PGMEA defines the structures (figure 3.5 **14**).

Second encapsulation in OSTE+ Flex At this point, a second 4 µm encapsulation layer of OSTE flex is deposited via spin-coating, UV-patterned trough MLA150 system and cured following the same procedure as for the first encapsulation layer, with the only difference that the electrodes are kept open and the photovoltaic cells are sealed. At this stage, the device is encapsulated within a layer of PI and a layer of OSTE flex, as depicted in figure 3.5 **15**. A top schematic top view of the final device is depicted in figure 3.5 **B**.

3.2.2 Final prototype process flow

The final process flow is an optimized version of the first proposed process flow, therefore some steps have been maintained equal. In the following description, when needed the differences are highlighted.

Surface cleaning and activation Similarly to the first proposed process flow, the surface of the 4 inches glass wafer is cleaned and activated through an oxygen plasma, which enhances the adhesion of the substrate material to the glass. Again, for our purposes the devices do not need to be released. In the future it will be needed to implement a sacrificial layer in order to easily detach the substrate from the wafer.

OSTE+ CC substrate spin-coating After surface preparation, a 10 µm substrate layer of OSTEMER^{TM} 322 Crystal Clear supplied by Mercene Lab, or OSTE+ CC, is spin-coated on the wafer, partially cured in a UV box and eventually it is thermally cured overnight to complete its polymerization (figure 3.8 **1**). The substrate is let to cool down with a gradual ramp down.

Photolithography - ITO bottom layer Once the substrate has been cured, the ring-shaped anodes, the bottom electrodes of the photovoltaic cells and the 6 bottom measurement pads are patterned onto a 2 µm layer of AZ$^{®}$1512 by means of the Maskless Aligner MLA150 (figure 3.8 **2**). The mask depicted in figure 3.6 and made in CleWin5 is the MLA mask design implemented at this photolithographic step.

ITO sputtering and lift-off After development of the photoresist, 200 nm of ITO are deposited via sputtering exploiting the AC450CT sputtering system (figure 3.8 **3**). The exceeding material is removed with a lift-off process in PGMEA under continuous sonication (figure 3.8 **4**).

PEDOT:PSS and PCPDTBT:PCBM spin coating Similarly to the first process flow, the polymers should be deposited via spin-coating and thermally cured in a inert atmosphere. First, 1 mL of PEDOT:PSS is spin-coated and cured for 30 minutes at 110 °C, then the source of the heat is turned off and the wafer is let to cool down naturally with a slow ramp down (figure 3.8 **5**). In second place, 35 µL of PCPDTBT:PCBM in chlorobenzene solution are poured and spin-coated above the second layer (figure 3.8 **6**). Consequently, the wafer is cured for 30 minutes at 110 °C and again let to cool down with a slow ramp down. The wafer is left in glove-box overnight.

Ti sputtering through shadow mask Similarly to the first prototypes microfabrication, a shadow mask is applied onto the wafer and aligned. The mask is used for Ti sputtering on the area of the photovoltaic cells to complete the stack of materials composing the cells (figure 3.8 **7**).

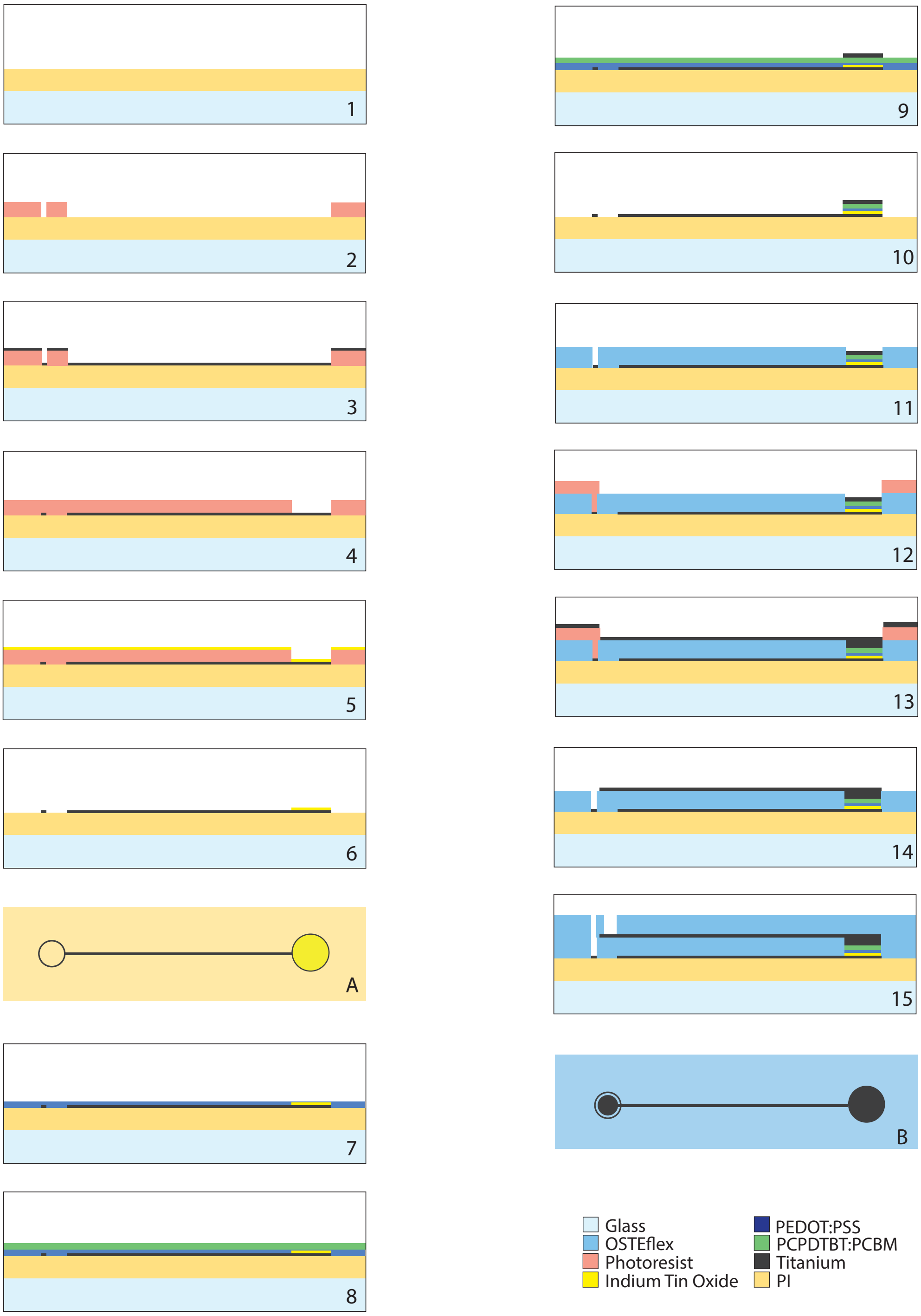

Figure 3.5: Graphic process flow: prototype 1

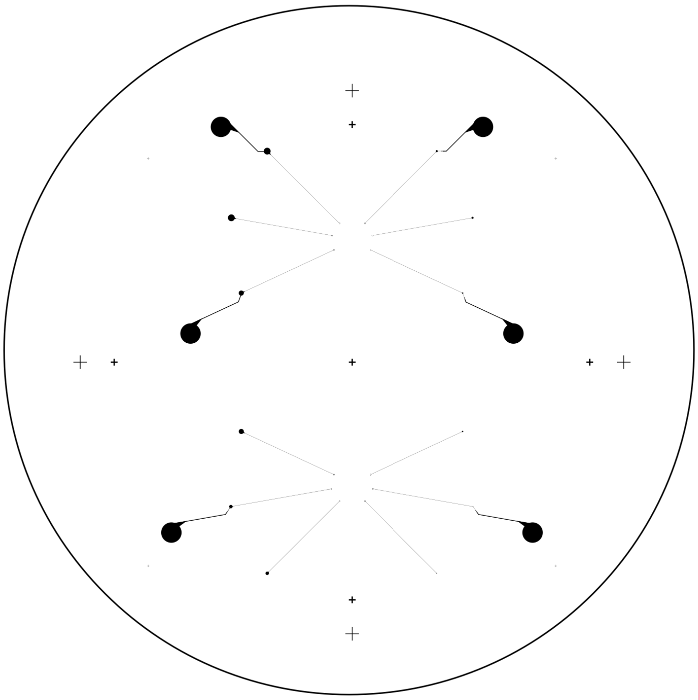

Figure 3.6: Mask design implemented for bottom layer patterning and ITO deposition. The mask was drawn implementing the software CleWin5 and it was used to pattern the photoresist AZ® 1512 with MLA150 by Heidelberg Instruments.

Polymers etching As above, the polymeric layers are etched through a RIE process, while they are preserved below the titanium layers deposited through the shadow mask (figure 3.8 **8**).

First encapsulation in OSTE+ Flex The first encapsulation is constituted by a 5 µm OSTE flex layer which is deposited by spin-coating on the wafer. The OSTE flex film is patterned with MLA, developed in Ethyl L-lactate, but here, differently from the first proposed process flow, the curing consists of 14 hours of baking at 100 °C and a natural slow cool down (figure 3.8 **9**). This expedient is used in order to avoid an abrupt transition from 100 °C to room temperature: being OSTE flex fairly flexible and highly affected by temperature [2] fast coolings can cause metal layers to delaminate or crack due to residual stress. A very slow and natural cool down can help to release the stress during the long time of temperature ramp down.

Photolitography - Pt and IrOx top layer A second photolithographic step performed with MLA150 allows to pattern the shapes of the electrodes top layer and measurement pads into a 2.5 µm layer of AZ® 1512 photoresist (figure 3.8 **10**). The MLA mask used at this step is depicted in figure 3.7.

---

[2] Note that OSTE flex glass transition temperature is 70 °C and that its shrinkage during cure is about 1%. This means that it contracts and expands easily with respect to relatively low temperatures endowing deposited layers with residual stress

Pt and IrOx sputtering After development of the photoresist, a 150 nm film of platinum is deposited through sputtering (figure 3.8 **11**). Once Pt sputtering is complete, a PI shadow mask is placed on the wafer, as it is shown in the side view in figure 3.8 **12** and in the top view of the device in figure 3.8 **B**. The mask shows apertures in the areas of the electrodes, so SIROF is sputtered on this regions only (figure 3.8 **13**). This expedient helps to eliminate one extra step of photolithography. The mask is then removed and the wafer is subjected to a step of lift-off aiming at lifting-off both the unwanted Pt and SIROF previously deposited (figure 3.8 **14** and **15**).

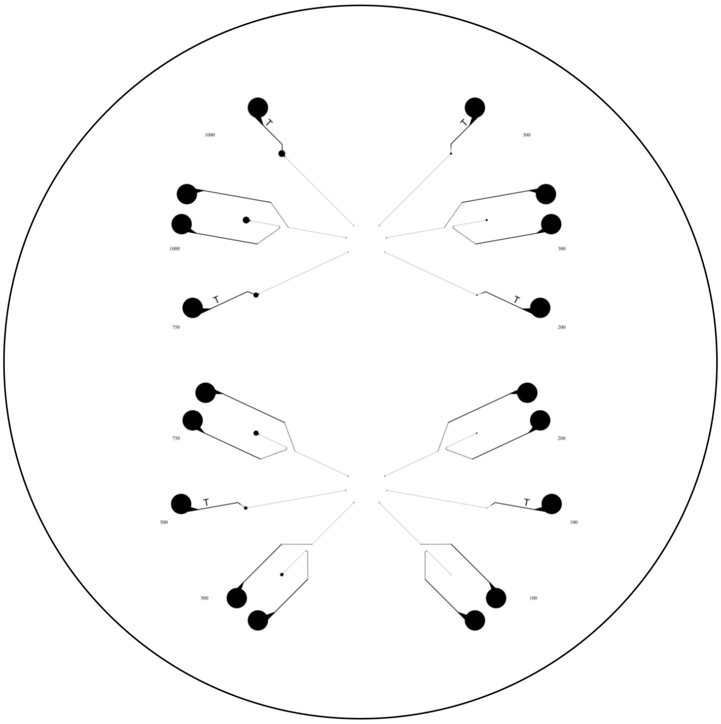

Figure 3.7: Mask design implemented for top layer patterning and Pt deposition. The mask was drawn implementing the software CleWin5 and it was used to pattern the photoresist AZ$^{®}$1512 with MLA150 by Heidelberg Instruments.

Second encapsulation in OSTE+ Flex At this point, a second 4 µm encapsulation layer of OSTE flex is spin-coated, exposed trough MLA150 system and cured for 14 hours at 100 °C (figure 3.8 **16**). As above a slow cool down is of paramount importance to preserve the deposited films from cracking or delamination. At this stage, the device is complete and totally encapsulated except for the Iridium Oxide surface of electrodes, which will be exposed to the neural cells once implanted.

3.3 From the first to the optimized prototype

The first and the last process flows have just been introduced. As briefly mentioned above, the wafers have been virtually divided into four batches which are related to important modifications of the process flow. Hereunder, the four groups are briefly presented and the main differences are highlighted.

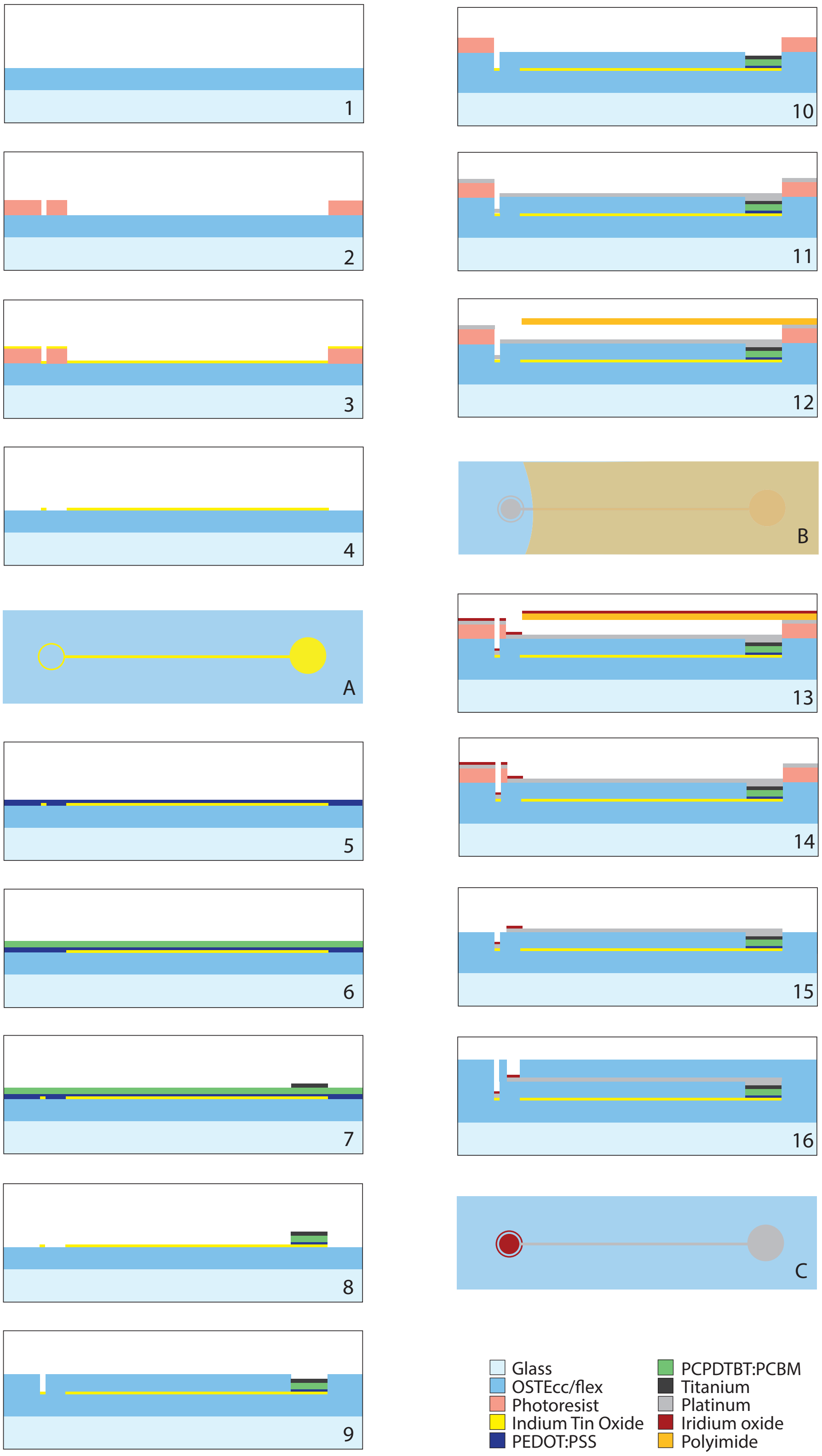

Figure 3.8: Graphic process flow: final prototype

First batch The first batch has been the starting point of this work. The process flow related to these first wafers is presented in section 3.2.1. To sum up, this batch is characterized by a polyimide (PI2611) substrate, a bottom layer composed by the presence of two different materials (Ti and ITO), the materials stack for the photovoltaic cell, 100 nm of sputtered Ti through a shadow mask, a first OSTE+ Flex encapsulation, a top layer entirely built in Ti and a final OSTE+ Flex encapsulation. No particular treatments have been implemented for bakings and developments: these processes have been performed with state-of-the-art or data-sheets standard recipes.

Second batch The second batch has been produced directly on the glass wafer: no substrate material has been implemented for this batch. It is characterized by a bottom layer entirely built in ITO as a substitute to the hybrid Ti-ITO bottom layer of batch one. The photo-active materials stack remained the same as for batch 1. The thickness of the Ti layer sputtered through the shadow mask has been modified from 100 nm to 300 nm. The first encapsulation has not been varied, except for the development procedure parameters. The top layer has been subjected to a substantial modification by using Pt instead of Ti. The final encapsulation has been subjected to the same development optimization as the first one. Standard recipes have been kept for bakings and coolings, while OSTE+ Flex development have been modified to an optimized procedure.

Third batch The third batch has been built on a OSTEMER^{TM} 322 Crystal Clear, referred to as OSTE+ CC, substrate layer. Concerning the materials implemented in the following steps, the entire stack has been kept as in batch 2, but a final SIROF layer deposited on the cathode and anode outer surfaces has been added. Although a large part of the materials have been maintained as in batch 2, the production of batch 3 has been characterized by the optimization of secondary procedures such as bakings and coolings, as well as sacrificial layers thickness.

Fourth batch The fourth batch of prototypes is the highest grade of optimization that could be achieved during this project. The entire materials sequence has been maintained as in batch 3. However, the number of photolithographies and a lift-offs have been reduced by integrating Pt and IrOx deposition in a single sputtering step. Moreover, a strong attention has been paid to fabrication steps of secondary importance, though fundamental for the success of the process flow, such as bakings and coolings, OSTEMER layers curing and shadow mask production and positioning.

3.3.1 Summary: from prototype 1 to prototype 4

For sake of simplicity, hereunder a sum up of the materials stacks and process optimization from batch 1 to 4 is proposed. For each group a table containing materials (in order of deposition) and related thickness is presented, as well as a list of minor process optimizations.

1st batch

- Materials sequence and relative thicknesses:

Material	Thickness
Glass wafer	500 µm
PI2611	10 µm
Ti	200 nm
ITO	200 nm
PEDOT:PSS	N.A.
PCPDTBT:PCBM	N.A.
Ti	100 nm
OSTE+ Flex	5 µm
Ti	150 nm
OSTE+ Flex	4 µm

2nd batch

- Materials sequence and relative thicknesses:

Material	Thickness
Glass wafer	500 µm
ITO	200 nm
PEDOT:PSS	N.A.
PCPDTBT:PCBM	N.A.
Ti	300 nm
OSTE+ Flex	5 µm
Pt	150 nm
OSTE+ Flex	4 µm

- Secondary steps optimization:
  - Modification of the design: starting from this batch the cells have been produced in 6 different sizes instead of being all 2.5 µm in diameter
  - OSTE+ Flex development: ethyl L-lactate, 60 rpm, 5 min

3rd batch

- Materials sequence and relative thicknesses:

Material	Thickness
Glass wafer	500 µm
OSTE+ CC	10 µm
ITO	200 nm
PEDOT:PSS	N.A.
PCPDTBT:PCBM	N.A.
Ti	300 nm
OSTE+ Flex	5 µm
Pt	150 nm
OSTE+ Flex	4 µm
SIROF	300 nm

- Secondary steps optimization:
  - OSTE+ Flex second curing step: 100 °C overnight + slow ramp down to RT
  - AZ1512 soft baking (for lithographic steps): 110 °C, 2 min, not contact + slow ramp down to RT
  - AZ1512 thickness for Pt sputtering/lift-off: 2.5 µm

4th batch

- Materials sequence and relative thicknesses:

Material	Thickness
Glass wafer	500 µm
OSTE+ CC	10 µm
ITO	200 nm
PEDOT:PSS	N.A.
PCPDTBT:PCBM	N.A.
Ti	300 nm
OSTE+ Flex	5 µm
Pt	150 nm
SIROF	300 nm
OSTE+ Flex	4 µm

- Secondary steps optimization:
  - OSTE+ Flex second curing step: 100 °C, 14 h, uniform heat source + slow ramp down to RT
  - Shadow mask material: PI Kapton supplied by DuPont (50 µm)
  - Clouding reduction (shadow mask)

3.4 Electrochemical characterization

Once fabricated, the functioning of the electrodes has been tested by impedance spectroscopy (IS) and cyclic voltammetry (CV) by means of a three-electrode potentiostat supplied by Ivium technologies. The set up comprises a Pt counter electrode and a Ag/AgCl reference electrode immersed in an electrolytic solution (here saline solution) while the working electrode has been connected with a gold spring contact embedded on a 3D printed holder, as shown in figure 3.9. A falcon tube has been cut and glued to the wafers with PDMS in order to confine the saline solution to the area of the electrodes.

3.4.1 Impedance spectroscopy

Impedance spectroscopy, as the name suggests, is a study which relates the quantity impedance (Z) upon the frequency. Indeed, impedance spectroscopy allows to measure the impedance of an electrode, i.e. its I/V relation, by applying an alternate current or voltage over a range of frequencies. As a matter of fact the I/V relation for an electrode interfacing an electrolytic solution cannot be simplified to that of a resistor (for which this relation is linear), but it carries two pieces of information: the magnitude and the phase. With the magnitude being the magnitude of the impedance vector and the phase its imaginary part or, in other words, the angle by which current and voltage are out of

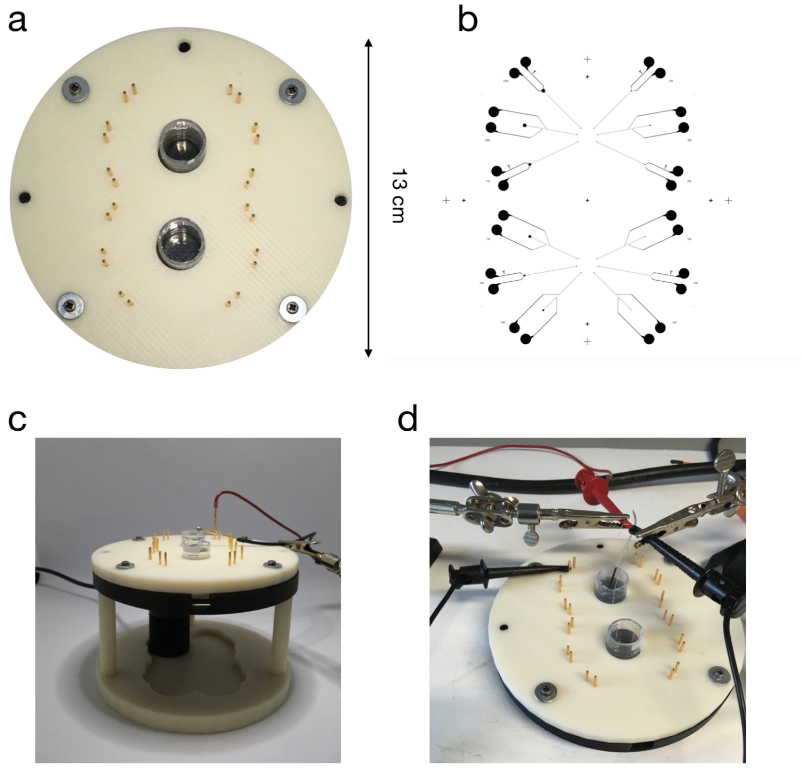

Figure 3.9: Experimental set-up for photovoltaic and electrochemical measurements: **a** Top view of 3D printed holder embedding 2 openings for falcon tubes containing saline solution and 24 gold spring contacts to connect the measurement pads. **b** Final wafers design. The position of spring contacts embedded on the 3D printed holder has been selected according to the position of pads on the design. **c** Photovoltaic measurement experimental set-up. The holder was sized to match LED height. The light emitted by the source reaches the cells through dedicated apertures in correspondence of cells position. **d** Experimental set-up for electrochemical measurements.

phase. The reason underlying its extensive implementation as a characterization technique for electrodic interfaces is the possibility to extract information about the reactions occurring at the electrode-electrolyte interface from the impedance analysis [34]. So, for instance, a non-working electrode would show an impedance modulus versus frequency plot more similar to that of an insulating material rather than a working electrode, both in shape and values. This is also true when plotting the phase with respect to the frequency. During this work, impedance spectroscopy measurements have been performed with a frequency ranging from 1 Hz to 1 MHz and a voltage of 50 mV.

3.4.2 Cyclic voltammetry

Cyclic voltammetry is a three-electrode electrochemical measurement aiming at extracting information about the oxidation and reduction reactions occurring at the electrode under test. Moreover, it provides information on the reversibility of these reactions and the stability of the electrodes [42]. During the acquisition, the potential of the test electrode is swept cyclically at a constant scan rate within a voltage window and with respect to the reference electrode. Current is allowed to flow between the electrode and the counter electrode. The shape of cyclic voltammetry cycles strongly varies with respect to the size of the electrodes, their shape and materials, so CV measurements are usually employed as a benchmark for stimulating electrodes. In this study, CV was performed with a test voltage sweeping from $-0.6\,\mathrm{mV}$ to $0.8\,\mathrm{mV}$ for six consecutive cycles with a scan rate of $50\,\mathrm{mVs^{-1}}$.

3.5 Photovoltaic characterization

The photovoltaic characterization of the cells consists in the acquisition of the photovoltage (photo-current) generated by the cell at the electrode with respect to the intensity of the light source. During measurements, the cell is illuminated through the transparent electrode with a NIR emitting LED supplied by Thorlabs with an emission peak of 730 nm. The voltage (current) is measured with a two-electrode system: the measurement pad, and thus the working electrode, is connected with a gold spring contact, while the voltage (current) at the electrode is measured with a Pt wire immersed in saline solution. The measurements of both photogenerated voltage and current were taken for various light intensities, triggered by a sweep in bias voltage from 0.1 V to 0.9 V with a step of 0.1 V and from 1 V to 5 V with a step of 1 V and a pulse duration of 10 ms. The data of LED irradiance ($\mu\mathrm{W/mm^2}$) versus bias voltage (V) are reported in figure 3.10 **a**, while the exact set of values in 3.10 **b**. Note that the experiments were carried out in complete darkness except for the LED light pulses.

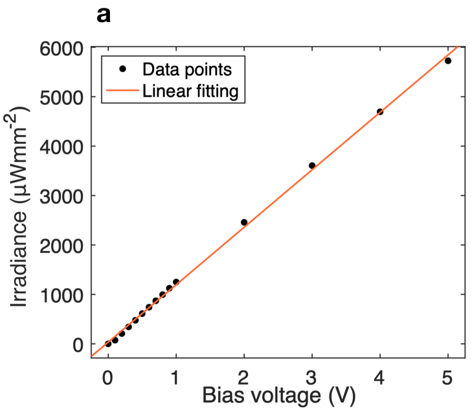

b

Bias voltage (V)	Irradiance ($\mu\mathrm{W/mm^2}$)
0.1	74.07
0.2	208.33
0.3	342.59
0.4	476.85
0.5	611.11
0.6	740.74
0.7	870.37
0.8	995.37
0.9	1125.00
1	1250.00
2	2458.33
3	3606.48
4	4694.44
5	5726.85

Figure 3.10: **a** LED irradiance versus bias voltage applied. Linear fitting of experimental data. **b** Experimental data.

3.5.1 Materials stack photovoltaic characterization through dedicated chips fabrication and testing

In order to understand the response of the materials stack theorized for the organic photovoltaic cells and to set a benchmark for further studies of the final devices, a set of chips have been fabricated. The chips show the same materials sequence proposed for the photovoltaic cells in the real devices, although they are much simpler in terms of fabrication and design. Hereunder, the process flow and the experimental set-up employed for the production and characterization of the chips.

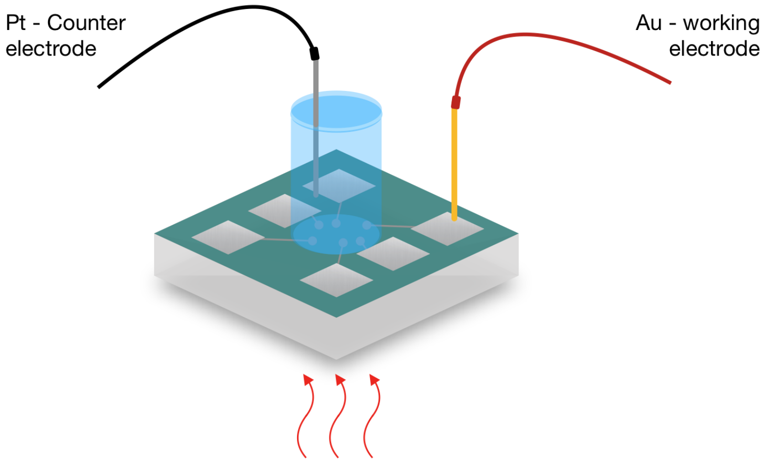

Figure 3.11: Measurement set up for materials stack photovoltaic characterization: chips are illuminated from the backside. The response is measured through a gold spring contact connected to the measurement pad and a Pt counter electrode immersed in saline solution.

Chips process flow A 4 inches glass wafer is first cleaned through an oxygen plasma. It is then subjected to HMDS surface preparation. Through a first photolithographic step, ITO sputtering and lift-off, the bottom layer in ITO is defined on the glass wafer. In glovebox, PEDOT:PSS and PCPDTBT:PCBM layers are spin-coated and cured following the standard procedure as in 3.2. A Ti layer defining the measurement pads, the traces and the electrodes is then sputtered through a shadow mask. The chips have no need for encapsulation or substrate layers.

Experimental set-up for photovoltaic testing After fabrication every chip has been tested. The set-up for photovoltaic measurements is reported in figure 3.11. The measurement pads have been connected through a gold spring contact, while the counter electrode has been immersed in saline solution. Similarly to the photovoltaic characterization of real devices, the cell was illuminated with a NIR emitting LED with the emission peak at 730 nm. The intensity of the LED was modulated through an increasing bias voltage from 0.1 V to 0.9 V with a step of 0.1 V and from 1 V to 5 V with a step of 1 V, resulting in the values of irradiance summarized in figure 3.10.

4 Results and discussion

In the following chapter the main results are reported and discussed. At the beginning, we present some preliminary results useful for the understanding of the following work. First the photovoltaic response given by the stack of photo-active materials on test chips and the ITO deposition optimized parameters are presented. After this brief introduction, each batch of fabricated wafers (see section 3.3) is analyzed from the point of view of the microfabrication challenges and relevant electrochemical characterization. Instead, the photovoltaic results will be discussed at the end of the chapter

4.1 Preliminary results

4.1.1 Materials stack photovoltaic response

In order to create a benchmark for the following study, the photo-voltage (PV) and photo-current (PC) have been measured upon illumination (730 nm) and in presence of saline solution as electrolytic medium. Figure 4.1 depicts an example of photovoltaic response collected from the measurement on one electrode. Figure 4.1 **a** shows the waveform of the photo-voltage generated by a sweep in light intensity as described in 3.5 and a pulse duration of 10 ms. As one can expect for a solar cell, the PV reaches a steady-state and remains constant until the source of illumination is turned off. Concerning the PC, in the example presented in figure 4.1 **b** it is possible to recognize a typical capacitive trend: when the light is shined on the photo-active material the current reaches its maximum and then it decays exponentially until the illumination is stopped. It is well known how Ti electrodes brought in contact with an electrolytic solution, contrarily to Faraidic mechanisms, mediate the transition from electronic current to ionic flow in a capacitive manner by charging and discharging the double layer at the electrode-electrolyte interface [9]. Therefore, we can conclude that the result is completely coherent with expectations. The PC and PV data from all the working electrodes[1] have been averaged and their standard deviation have been computed. The results for mean PC density peak (±s.e.m) and mean PV (±s.e.m) are displayed in figure 4.2 **a** and **b**, respectively. A monotonic increasing trend following an increase of LED intensity can be deduced from the observation of the resulting plots. The photo-voltage measured for the maximum irradiance, or rather 5727 $\mathrm{mWmm^{-2}}$, was 73.37±19.49 mV. Concerning the photo-generated current, the peak of current density at the highest irradiance was evaluated as $44.22 \pm 12.17\,\mu\mathrm{Amm^{-2}}$.

---

[1] The clearly non-functioning electrodes have been removed by the calculations in order not to misrepresent the results. We can attribute the disfunctionality of some electrodes to the presence of residuals of PDMS on the electrodes after falcon tubes gluing to the chip.

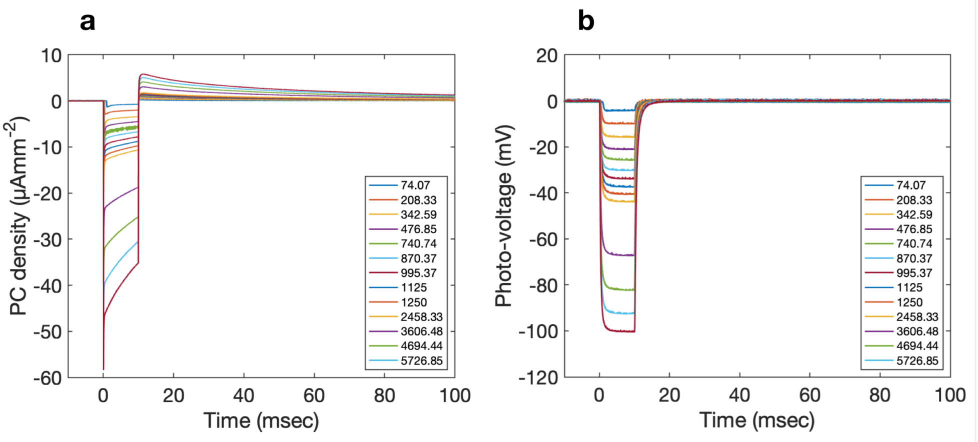

Figure 4.1: **a** Example of generated photovoltage and **b** example of generated PC density. The present measures have been collected from one electrode with a diameter of 100 µm at increasing LED intensity and pulse duration of 10 ms.

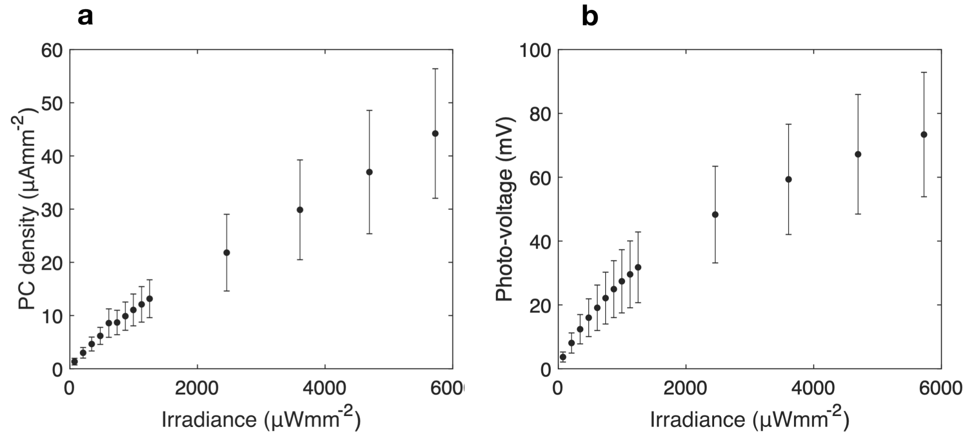

Figure 4.2: **a** Mean (±s.e.m) PC density and **b** mean photovoltage (±s.e.m). The data have been collected upon illumination (730 nm) with 10 ms pulses at increasing light intensities.

4.1.2 ITO deposition for optimized sheet resistance

As mentioned in section 3.1.3, ITO is largely exploited as electrodes material in OPV applications because of its transparency over a large range of the visible light spectrum and its good electrical conductivity. Both the above mentioned properties are desirable in OPV applications, but they inversely depend upon thickness. A trade-off is then required in order to maintain a good transparency to avoid losses on the anode and a fair electrical conductivity. However, ITO resistivity does not only depend upon film thickness, but it is also affected by sputtering parameters such as pressure and temperature as well as gas flow. Therefore, the deposition parameters need to be adjusted in order to match the specific requirements for the application. Temperature and pressure of operation are the most critical parameters affecting ITO conductivity, hence a detailed analysis has been carried out in order to set the optimal values. Experimental results of resistance versus pressure and temperature are displayed in figure 4.3 **a** and **b**, respectively. In particular, temperature is a parameter of primary importance in the framework of this study, since

Power	Ar flow	O2 flow	% Gas Share argon	Pressure	Temperature
150 W	26 sccm	1 sccm	96,29 sccm	$5 \cdot 10^{-3}$ mBar	20 °C

Table 4.1: Optimized parameters for ITO sputtering through AC450CT sputter system supplied by Alliance concept.

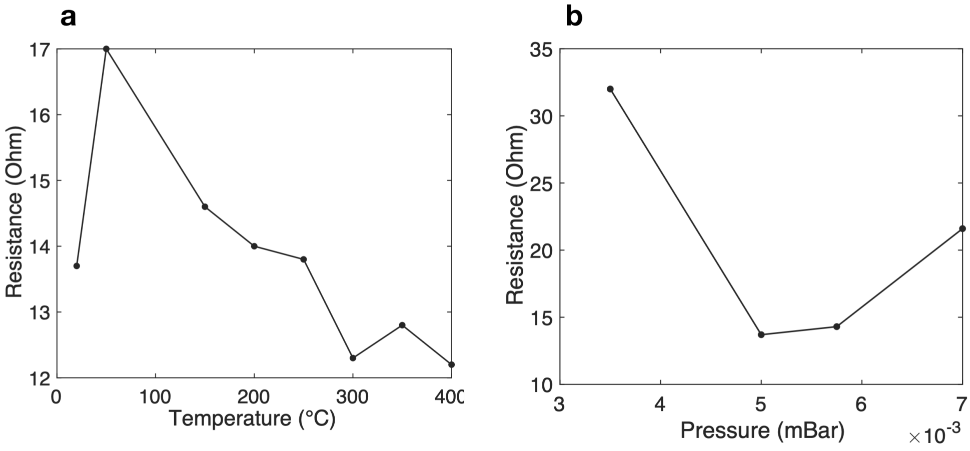

Figure 4.3: **a** 4 points resistance (Ω) of ITO sputtered films versus temperature (°). **b** 4 points resistance (Ω) of ITO sputtered films versus pressure (mbar).

ITO is to be deposited on polymers which are strongly affected by temperature variations[2]. Figure 4.3 **b** shows the values of 4 points resistance versus temperature acquired during the deposition tests. Although, towards very high temperatures the resistance drops, we still have to consider the constraints set by the underlying materials. Nevertheless, the resistance of the film deposited at 20 °C resulted to be 13.7 Ω which is negligibly higher than the resistance measured for 300 °C (12.3 Ω). Once the temperature has been set at 20 °C, the working pressure was investigated. In figure a clear minimum at $5 \cdot 10^{-3}$mBar. As a consequence, this result has been selected as optimal value. In addition, a set of experiments was performed to select the other deposition parameters. The final results are summarized in table 4.1.

4.2 Batch 1

4.2.1 Microfabrication results

The first batch of wafers was fabricated according to the process flow described in section 3.2.1. Many issues and challenges arose during this first microfabrication procedure. First of all, the development procedure in Ethyl L-Lactate of OSTE+ Flex after MLA150 exposure resulted to return poor results. After exposure with laser (375 nm), the wafer was soaked in Ethyl L-Lactate for 4 minutes on a shaker set at 80 rpm. The high rotational speed caused OSTE+ Flex detachment, allowing the liquid inside the OSTE layers. To better understand the mechanism, a microscope image of a measurement pad after

---

[2] Although the first prototypes have been fabricated on a polyimide substrate, which can withstand very high temperatures, these experiments have been performed with the clear aim to transit to OSTE+ CC as a substrate material. Indeed, OSTE+ CC is extremely sensitive to temperature, having a glass transition temperature of 75 °C [43]

OSTE+ Flex development is reported in figure 4.13 **c**. In the image we can observe how the OSTE+ Flex layer is detaching from the underlying layer and is being lifted-off by the rotational movement. Moreover due to this early side-effect, the development had to be stopped before the smaller features had completely been developed. A SEM image of one electrode after OSTE+ Flex development is reported in figure 4.13 **a**. The external ring appears to be only partially developed, so that residuals of OSTE+ Flex are found on the area of the electrode. Encapsulation materials are chosen for their dielectric properties, therefore incomplete development of the stimulating electrodes would imply a modification of the superficial area in contact with the biological tissue. A smaller area could mean inefficient stimulation or unexpected properties. Several trials had led to the final development procedure which consists in a 5 minutes soaking in ethyl L-lactate at 60 rpm. This procedure had been already employed for wafers of the same batch resulting in complete opening of both anode and cathode areas, as shown in figure 4.13 **b**.

One other major concern during fabrication of batch 1 was related to titanium sputtering over OSTE+ Flex encapsulation layer. To recall what is better explained in 3.3, Ti top layer is deposited via sputtering onto the OSTE+ Flex first encapsulation layer and it is then selectively removed through a lift-off step in PGMEA. To complete the production process, a second layer of OSTE+ Flex is deposited via spin-coating, it is patterned with MLA150 and then it is cured overnight at 100 °C. At the end of this procedure the titanium layer would show several cracks, as it can be noticed in figure 4.13 **d**. An explanation of this phenomenon can be given by referring to OSTE+ Flex and Ti mechanical properties as well as to the adhesion force between the two materials. OSTE+ Flex is a strongly temperature dependant polymer: its glass transition temperature is approximately 50 °C and it will become soft when exposed to temperatures above 80 °C, as stated in the product datasheet [44]. Moreover, it shows a shrinkage of about 1% during cure. This means that the polymeric layer shrinks every time the wafer is brought to its curing temperature and relaxes when going back to room temperature. On the other hand, Ti shows a very good adhesion to OSTE+ Flex layers which means that the metallic film tends to follow this shrinkage. Being poorly flexible, Ti cannot contract and relax but it rather generates cracks, which interrupt the conductive path. To avoid this undesirable effect, a crucial modification has been introduced in the process flow of the subsequent batch (batch 2): Ti has been substituted with Pt. Showing worse adhesion properties to OSTE+ Flex, Pt could possibly conform better to the substrate contractions and expansions at relatively high temperatures.

Figures 4.13 **e** and **f** reveal an additional problem. In particular the microscope images depict one photovoltaic cell top layer after first encapsulation in OSTE+ Flex. From an uncareful analysis of figure 4.13 **e** one could deduce that a particle or residuals of some previous processes have been left on the wafer. However, by observing figure 4.13 **f**, that was collected focusing on a different focal plane, it is possible to understand that the entire stack of the cell has been lifted-off. The lack of titanium on the cell means that doubtless both PCPDTBT:PCBM and PEDOT:PSS have been washed away with solvents so that no photo-active material was left in place. Recalling again a passage of the process flow: after the photo-active layers deposition and curing, a shadow mask was implemented to sputter 100 nm of titanium selectively on the photovoltaic cells and subsequently etch the polymers through this titanium "mask". The exposure of the 100 nm Ti "mask" to the etchant species probably reduced its thickness enough to crack it and easily cause delamination. Plausibly this effect was exacerbated by the development of OSTE+ Flex in ethyl L-lactate that washed away the residual flakes of Ti.

4.2.2 Electrochemical characterization

The electrochemical characterization was carried out in order to verify the assumptions made during the microfabrication. In particular, it was of interest to test the electrodes through impedance spectroscopy in order to assess or deny their functioning.
Figure 4.4 **a** and **b** report the average impedance module and phase measured for the bottom electrodes, i.e. the ITO anodes. Impedance module behaves as expected for usual working electrodes displaying a plateau at relatively low impedance (around 10 kΩ) for frequencies ranging between 10 kHz and 1 MHz. Even though, the impedance value results higher with respect to expectations, being already approximately 100 kΩ at 1 kHz. The impedance phase behaviour can also be recognized as a standard evolution showing an initial decrease from approximately −80° at 1 MHz towards −40° at 100 kHz and then increasing again before stabilizing at around −65° at lower frequencies.

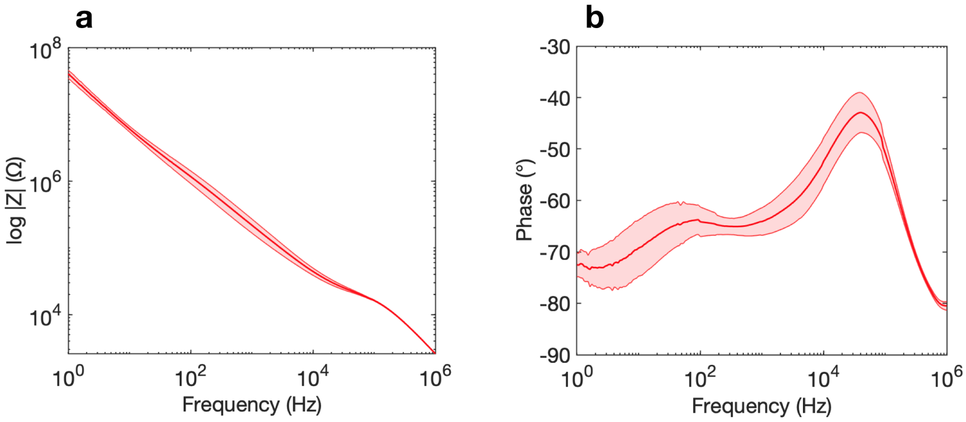

Figure 4.4: a Average impedance module and **b** average impedance phase of ITO/Ti bottom electrodes of batch 1 measured with frequency ranging within 1 Hz and 1 MHz at a voltage of 50 mV, utilizing the measurement set-up described in section 3.5.

Contrarily to what measured for the bottom electrodes, the top electrodes showed a different trend implying their non-functionality. Module and phase plots measured for Ti top electrodes are depicted in figure 4.5 **a** and **b**. Indeed, in the figure we can observe for five out of six electrodes a typical insulating behaviour. Impedance module measured for the electrodes 1, 2, 4, 5 and 6 increases steadily from the highest sinusoidal voltage frequency, 1 MHz, to the lowest, 1 Hz, without encountering any plateau. Furthermore, the impedance phase remains constant at −90° for a large range of frequencies and it shows random peaks at very low frequencies. This behaviour reconfirms the hypothesis of non-functionality made by observing the module evolution. Only one electrode out of six, in yellow in figure 4.5, follows a similar trend to what described for bottom electrodes.

4.3 Batch 2

4.3.1 Microfabrication results

Batch 2 was designed in order to allow the transition from PI substrate to OSTE+ CC substrate. For this reason, devices of batch 2 were built directly on glass in order to evaluate the impact of other process flow modifications without the influence of the substrate material. This batch was characterized by a bottom layer entirely built in ITO, instead

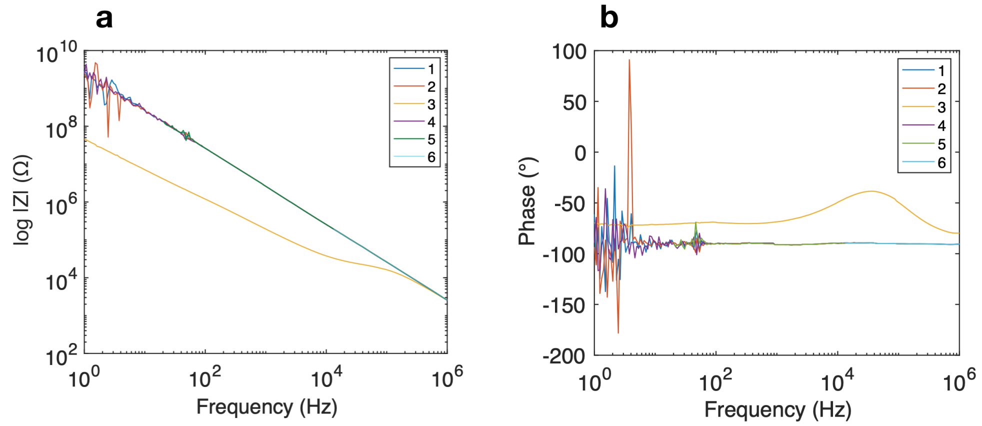

Figure 4.5: a Impedance module and **b** impedance phase of Ti top electrodes of batch 1 measured with frequency ranging within 1 Hz and 1 MHz at a voltage of 50 mV, utilizing the measurement set-up described in section 3.5.

of Ti and ITO together. This change did not particularly affect the process flow, on the contrary it was helpful in order to simply the entire procedure and to reduce the number of photolithographic steps. The second important modification was related to the top electrodes material. They were previously built in Ti, but due to cracking issues they have been fabricated with Pt in batch 2.

Concerning Pt deposition, it has been observed that, contrarily to Ti, Pt is more prone to adapt to OSTE+ Flex contractions and expansions without showing clear cracks. This tendency could be plausibly due to its worse adhesion to OSTE+ Flex. Although this feature led to an improvement from the standpoint of the cracking of top electrodes, it caused a large delamination of Pt during lift-off. Figures 4.14 **a** and **b** show Pt traces after development in PGMEA. As it can be observed, the lines do not show explicit cracks, but rather some sections seem lifted-off. We attributed this event to the long time of the lift-off procedure (almost 2 h) under continuous sonication which can cause detachment of layers with weaker bond strength. Along with lift-off and sonication, also fast coolings could contribute to aggravate this effect. A shorter time of exposure to solvents and sonication together with controlled coolings after baking could, indeed, produce better results.

Figure 4.14 **c** and **d** represent a second issue related to Ti sputtering over the photovoltaic cell. Remember that from batch 2 the design was slightly modified in order to test the microfabrication process and the devices performances with respect to different cell sizes and that 300 nm of Ti were sputtered instead of 100 nm. The images have been taken after polymers etching. As described in the previous chapter, Ti is sputtered on the photovoltaic cells through a shadow mask and it is then exploited to cover the cells area not to be damaged during RIE. In the optical microscope images we can observe an unwanted Ti shadow around the photovoltaic cell. The only possible hypothesis to explain this effect is that the shadow mask was not in perfect contact with the underlying polymers entailing a "clouding" effect under the mask. This issue, together with an intrisic tilting of the sputtering set-up, endowed this mediocre result. Furthermore, the shape of the cell can be recognized through the Ti layer. Ti films are usually opaque and thus it would be normal not to perceive any shape behind Ti layers. As a consequence, we should conclude that only a very thin layer of Ti was deposited. This is not hard to believe, if we recall that Ti was sputtered through a shadow mask showing features of maximum

1000 µm. Shadow masks intrinsically cause loss of material, for instance on the walls of the features. It has already been stated that a too thin layer of Ti cause cracking and delamination of the cell after lift-off or any other wet process. Figure 4.14 **e** and **f** show two different sizes of PV cells after second encapsulation in OSTE+ Flex having lost part of the cell top layer and thus exposing the polymers to the outer environment.

4.3.2 Electrochemical characterization

Batch 2 was fabricated on a glass wafer without any additional substrate layer. As a consequence, bottom electrodes were not subjected to any crucial procedure. Moreover, since the OSTE+ Flex development had been adjusted in order to ensure complete opening of the electrodes, the entire area of the anular anodes was exposed to the electrolytic solution.

Figure 4.6 **a** and **b** show results of impedance module and phase. Again, in the module plot we can recognize the evolution followed by typical working electrodes in response to an applied AC voltage input: starting from 1 MHz and lowering the frequency, the curve first encounters a plateau within 100 kHz and 1 kHz stabilizing at a value of approximately 30 kΩ. After the plateau the curve tends to increase steadily until the lowest frequency, i.e. 1 Hz. Comparing the results of batch 2 with batch 1, we observe that the behaviour of the bottom electrodes is similar, particularly in shape. Regarding impedance module values, batch 2 resulted in a slightly lower impedance at 1 kHz, being a few tens of kHz. From the point of view of the phase, the trend is again analogous to what observed for batch 1. Even though in this second case, phase reaches lower values around −20° at 10 kHz instead of −40°.

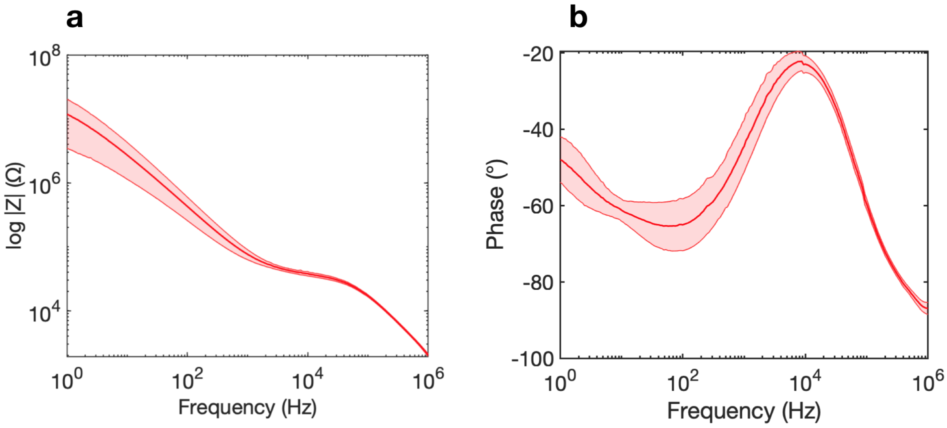

Figure 4.6: **a** Average impedance module and **b** average impedance phase of ITO bottom electrodes of batch 2 measured with frequency ranging within 1 Hz and 1 MHz at a voltage of 50 mV, utilizing the measurement set-up described in section 3.5.

Starting from batch 2 the top electrodes have been built in Pt for substituting Ti that was cracking due to residual stress caused by the underlying OSTE+ Flex layer. In figure 4.7 we can find both impedance module **a** and phase **b** of top electrodes made out of Pt and tested through an AC voltage input. In both plots, a clear division between functional and dysfunctional electrodes can be recognized. Non-working electrodes show the typical, almost linear, steady increase from 1 MHz to 100 Hz and random values at lower frequencies. Moreover, dysfunctional cathodes show very high impedance, about 10 MΩ, at 1 kHz. On the contrary, working electrodes evolve over the window of test frequencies with a well-known behaviour: an increase for very high frequencies (1 MHz), a plateau within 100 kHz and 1 kHz followed by an increase until 1 Hz. Pt electrodes showed a lower impedance with respect to ITO electrodes, reaching values close to 10 kΩ at 1 kHz. The phase, depicted in figure 4.7 **b**, follows the same trend as for bottom electrodes, but resulting in slightly different values: it starts at −50° at 1 MHz, proceeds to higher values until it reaches almost 0° at 100 kHz and subsequently goes back to lower values for lower frequencies.

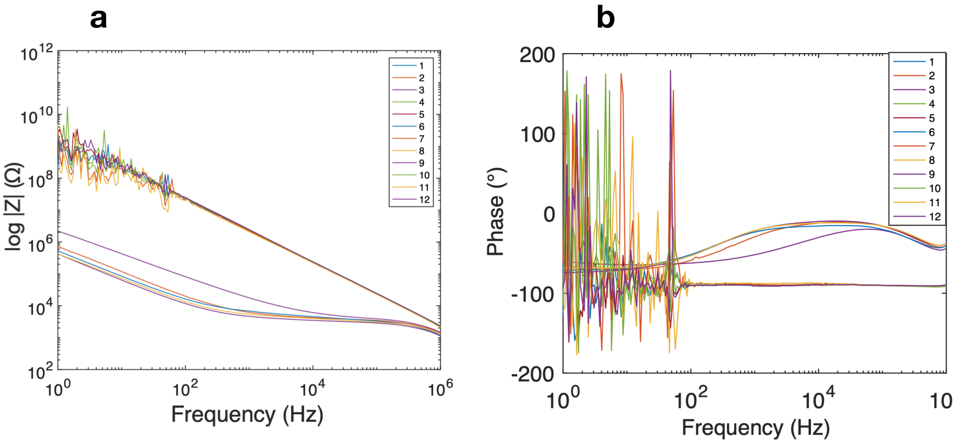

Figure 4.7: **a** Impedance module and **b** impedance phase of Pt top electrodes of batch 2 measured with frequency ranging within 1 Hz and 1 MHz at a voltage of 50 mV, utilizing the measurement set-up described in section 3.5.

4.4 Batch 3

4.4.1 Microfabrication results

Batch 3 defines the transition to an entirely flexible OSTEMER based device. One of the biggest challenges that were solved during batch 3 fabrication regarded the top Pt layer delamination. As hypothesized during the fabrication of batch 2, Pt delamination could be caused by the long time of lift-off in solvents plus sonication together with fast non-controlled coolings. A major modification of the process flow for batch 3 production, indeed, regarded the standardization and control of cool down processes. Each bake, comprising photoresist soft bakes and OSTE layers curing, was followed by a slow ramp down to room temperature in order to mitigate the effect of shrinking of the OSTE layers. Furthermore, a second precaution was taken specifically for the Pt top layer: a 2.5 µm film of AZ® 1512 was exploited as a sacrificial layer in order to enlarge the exposed area of photoresist to the solvent and thus to speed up the lift-off process. An example of successful lift-off and encapsulation is shown in figure 4.15 **e**.

As anticipated above, batch 3 wafers were fabricated on top of a OSTE crystal clear substrate layer. The first tests of ITO deposition onto the new substrate are displayed in figures 4.15 **a** and **c**. As it can be observed the ITO film shows a wavy pattern both on large and small features. However, this phenomenon affected only a portion of the devices embedded on the wafers, while the other, as depicted in figure 4.15 **b** and **d**, was uniform and smooth. In order to understand the nature of such texture the features were tested through a Bruker's Dektak® stylus profiler. Interestingly, the features showing the wavy texture were found to be at a lower level with respect to the OSTE+ CC level. After a detailed analysis of the curing procedure, we have been able to evaluate that the issue was generated by a non-uniform curing of the substrate layer due to an inhomogeneous thermal distribution of the hotplate employed for that procedure.

Once the major problems related to the process flow had been solved, a last photolithographic step was introduced. As anticipated in section 3.1.2, in order to improve the CSC of the electrodes a SIROF coating has been added on both anode and cathode. Unfortunately, the additional lithographic step on top of the last encapsulation layer resulted in a non-uniform coating, as it is shown in figure 4.15 **f**. We attributed this result to the high aspect ratio of the electrodes.

4.4.2 Electrochemical characterization

The electrochemical analysis of batch 3 was mostly related to ITO bottom electrodes in order to understand the influence of the substrate layer on their performances. In particular, we have analyzed electrodes built on a non-homogeneously cured OSTE+ CC layer and compared them to electrodes built on uniformly cured substrates. Figure 4.8 depicts the impedance module **a** and phase **b** obtained for ITO bottom electrodes deposited on a partially cured OSTE+ CC layer due to a non-uniform heat distribution of the heat source. Only half of the bottom electrodes can be considered as functional, in particular we can recognize the well-known trend followed by typical functional electrode in curves 1, 2 and 6. On the contrary, other electrodes show a steady increase, typical of non-working electrodes. Interestingly, by comparing the obtained data with the optical images of the wafer, it was found that the non-functional electrodes according to the impedance spectroscopy corresponded to the ones that have collapsed below the level of the OSTE+ CC layer, as for example in figure 4.15 **a** and **c**.

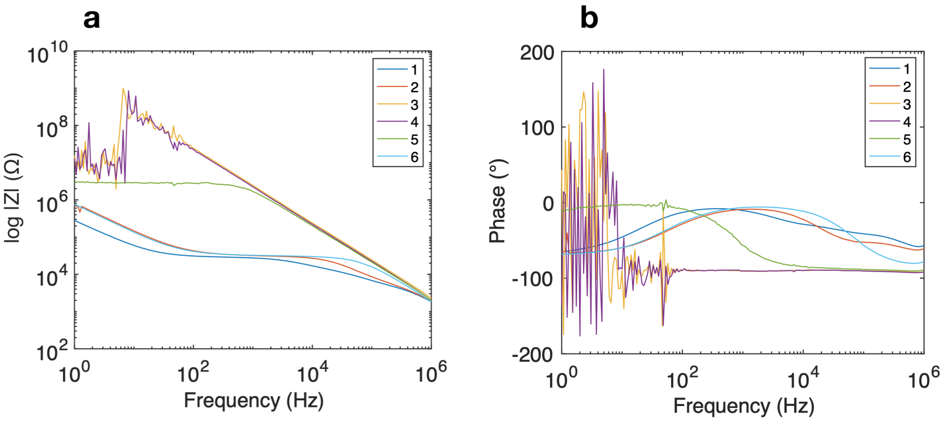

Figure 4.8: **a** Impedance module and **b** impedance phase of ITO bottom electrodes of batch 3 built on a non-uniformly cured OSTE+ CC substrate measured with frequency ranging within 1 Hz and 1 MHz at a voltage of 50 mV, utilizing the measurement set-up described in section 3.5.

Once the curing process of OSTE+ CC has been standardized and the heat inhomogeneity issue solved, further studies have been carried out on ITO electrodes. New wafers belonging to batch 3 were produced according to the new procedure. First the ITO patterned film was investigated via optical microscopy and Bruker's Dektak® stylus profiler. The ITO surface did not reveal the wavy pattern, depicted in picture 4.15 **a**, which is an indication of structures collapse. Moreover, the hypothesis was corroborated by profilometer measurements that confirmed that the ITO layer was on a higher level with respect to OSTE+ CC. The results of the electrochemical characterization are reported in figure 4.9 where we can appreciate the usual behaviour of ITO electrodes.

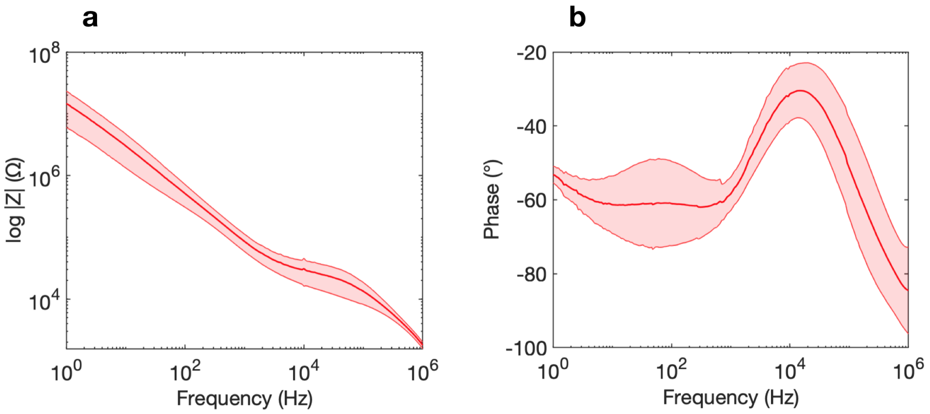

Figure 4.9: **a** Average impedance module and **b** average impedance phase of ITO bottom electrodes of batch 3 built on a uniformly cured OSTE+ CC substrate measured with frequency ranging within 1 Hz and 1 MHz at a voltage of 50 mV, utilizing the measurement set-up described in section 3.5.

4.5 Batch 4

4.5.1 Microfabrication results

During batch 3 fabrication, we have achieved a fair level of optimization of the process flow. Batch 4 aimed at obtaining a final process flow with standardized and reproducible steps. In particular OSTE+ Flex baking and cooling procedures have been automatized, while the uniformity of the curing have been achieved by ensuring a better and uniform contact of the wafer with the heat source.

A few challenges were still open at the time of batch 4 production. The most critical were SIROF deposition, which resulted in a failure for batch 3, and Ti sputtering through the shadow mask.

Starting from Ti deposition, a new technique was investigated: instead of using a rigid silicon mask, a PI mask was implemented to conform better to the underlying polymeric layer. Despite at the moment of the alignment the mask would adhere to the polymers, the final result was similar to what obtained with the silicon mask. Only few cells resulted to be evenly coated. The main problem related to the PI mask lies in the fact that metal sputtering generates a stress on the upper surface of the mask where the material is deposited. This stress forces the mask to bend and thus to detach from the wafer. Figure 4.16 **a** and **b** depict two opposite results obtained with a PI mask: the first one showing the usual Ti shade and optical transparency, the second a more defined and opaque coating.

In order to avoid an additional unnecessary lift-off step, that can always be critical for the underlying layers, and to deposit SIROF on a relatively low aspect ratio surface, two photolithographic steps have been integrated. In particular, Pt and SIROF were deposited together before being encapsulated with the second encapsulation layer in OSTE+ Flex. A shadow mask was produced in order to be placed on the wafer after Pt deposition to

cover the traces and the cells. Figure 4.16 **c** depicts the moment of mask alignment after Pt and before SIROF deposition. The final result, displayed in figure 4.16 **d**, was positive since all the electrodes were uniformly coated and no sign of metal lines detachment could be found.
After IrOx successful sputtering and lift-off, the material surface was characterized via SEM. Figures 4.16 **e** and **f** depict a close up on the electrode surface and the entire electrode, respectively. Even though we expected SIROF to show a higher porosity, the roughness of the surface still helps to enhance the CSC of the electrodes by enlarging the electrochemical surface area with respect to the geometric surface area. By analyzing the SEM pictures we have evaluated that the surface motif is generated by a pronounced granularity with features ranging within 30 nm and 150 nm.

4.5.2 Electrochemical characterization

As anticipated above, the new procedure in order to avoid an additional step of photolithography returned positive results in terms of resolution and uniformity of the films. Therefore, the final coating of SIROF was tested through cyclic voltammetry to evaluate the behaviour of the electrodes and to compare them with non-coated ones. Here we report the resulting average curve for cathodes: figure 4.10 **a** depicts the cyclic voltammogram for top electrodes built in Pt, while **b** depicts the same measurement carried out for SIROF-coated Pt electrodes. From a first visual inspection of the shape of the curves, we can already observe their profound difference. In 4.10 **a** the loop is narrow and subtends a small area. Moreover it reaches its maximum through a steep and steady increase. On the contrary, figure 4.10 **b** shows a large area under the curve. Differently from **b**, here the curve reaches the maximum and then remains constant over a relatively large potential window which is a typical behaviour for electrodes with large electrochemical surface area. From a quantitative point of view, curve **a** reaches an anodic current peak value of approximately 2.5 nA at maximum potential versus Ag/AgCl counter electrode, while the cathodic reaches approximately −1.5 nA. Curve **b** shows much higher current peaks instead, resulting in a cathodic and anodic current peaks close to 500 nA in module.

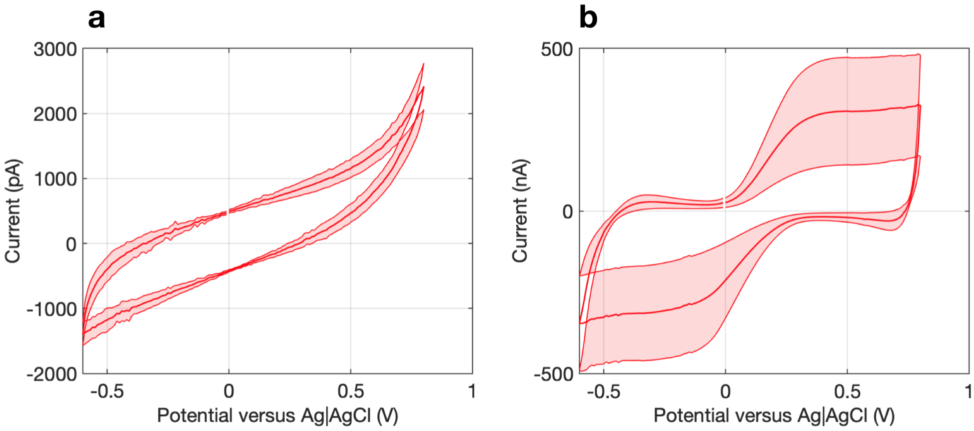

Figure 4.10: **a** Cyclic voltammetry of Pt top electrodes **b** Cyclic voltammetry of SIROF top electrodes measured with test voltage sweeping from −0.6 mV to 0.8 mV for six consecutive cycles with a scan rate of 50 mVs^{-1}

One fundamental parameter is the charge storage capacity (CSC), which is calculated from the time integral of the partial current during a complete potential cycle, and gives information on the quantity of charge available at the interface for stimulation. The CSC has been computed for Pt and SIROF electrodes, both for anodic and cathodic partial currents, and it is reported in figure 4.11 **a** and **b**. Concerning Pt electrodes, an average anodic CSC of 0.09 $\mathrm{mC/cm^2}$ and a cathodic CSC of 0.10 $\mathrm{mC/cm^2}$ were measured. For SIROF-coated electrodes, instead, the anodic CSC was evaluated to be 34.80 $\mathrm{mC/cm^2}$, while the cathodic 35.40 $\mathrm{mC/cm^2}$. Even though from the SEM analysis of SIROF the surface looked smoother than expected, we can conclude that the sputtering of IrOx on the electrodes brought positive results by enhancing the CSC of Pt electrodes.

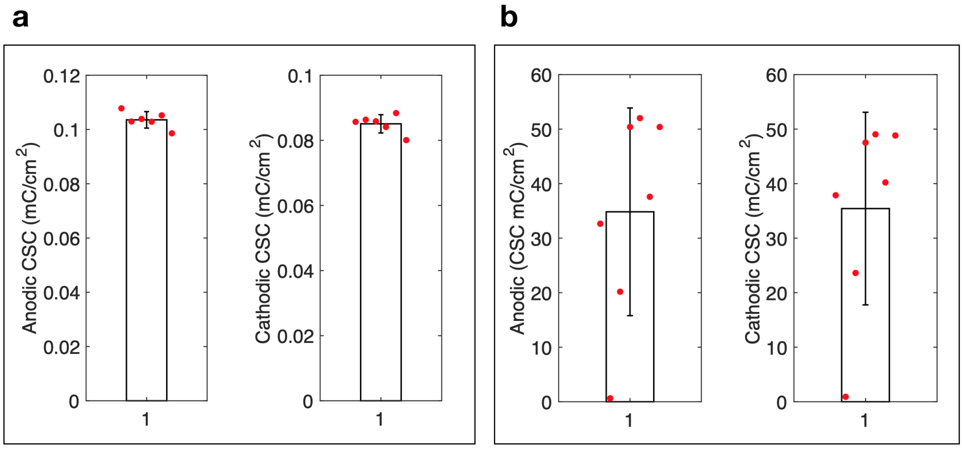

Figure 4.11: **a** Charge Storage Capacity of Pt top electrodes **b** Charge Storage Capacity of SIROF top electrodes

4.6 Photovoltaic characterization

We have already commented upon PCPDTBT:PCBM photovoltaic response in section 4.1.1. Through the production and testing of dedicated chips, we have been able to measure an average photovoltage of 73.37 ± 19.49 mV and a peak current density of 44.22 ± 12.17 $\mu\mathrm{Amm^{-2}}$ at maximum LED irradiance (5727 $\mathrm{mWmm^{-2}}$). Photovoltaic characterization has been carried out during the optimization of the process flow of the real prototypes in order to evaluate the condition of the polymers after the microfabrication procedure and to test the correct deposition of materials. It was of particular interest to explore the influence of the encapsulation layer deposition and patterning on the photovoltaic cell, as well as the Ti layer thickness variations.

Throughout this experimental work, many photovoltaic cells have been tested as described in 3.5. However, the responses we obtained were strongly variable in waveform and in photo-voltage and photo-current peak values.

Concerning batch 1, many photovoltaic cells could not be tested due to the critical issue of Ti traces cracking onto OSTE+ flex layers. Moreover, the detachment of Ti flakes from the top layer allowed the entrance of solvents and developers into the cells and thus in contact with the photo-active polymers.

Batch 2, on the other hand, was the starting point for OSTE+ CC integration, but it still suffered of major problems. To cite one example that certainly affected the photovoltaic response, the thickness of the Ti layer sputtered through the shadow mask was far from being the expected one by clearly showing transparency and cracking of the metal layer.

During fabrication of batch 3, positive results in terms of microfabrication were obtained,

even though it was hardly possible to solve the problem of the shadow mask generating a huge mismatch within the expected thickness of Ti and the real one.
Batch 4, as mentioned above, was the highest level of optimization we could reach at the end of the project. To overcome the challenge set by the silicon shadow mask, we have produced a 50 µm thick Kapton® PI mask by cutting the features with laser-cutter. Unfortunately the bending of the PI mask caused again loss of material during sputtering. However, few of the cells were evenly coated. The results of the photovoltage characterization, however, where still quite poor. The best photovoltaic response given by the 1000 µm diameter cell and measured with respect to the top Pt/SIROF electrode is reported in figure 4.12 **a** and **b**. As we can deduce from the graph, the waveform of photovoltage is not exactly what expected from a solar cell. Normally, the PV should encounter a steady-state as long as the illumination is on. Here, on the contrary, decreases in a quasi-exponential manner. Even though, the maximum of PV, being 53.27 mV, is quantitatively coherent with the average computed for the chips. From the point of view of the PC density, the waveform follows the same trend as what measured for the chips in section 4.1.1, but displays a faster decay. Moreover, the resulting peak value, or 9.17 μAmm^{-2}, is much smaller than the reference value measured on the chip.

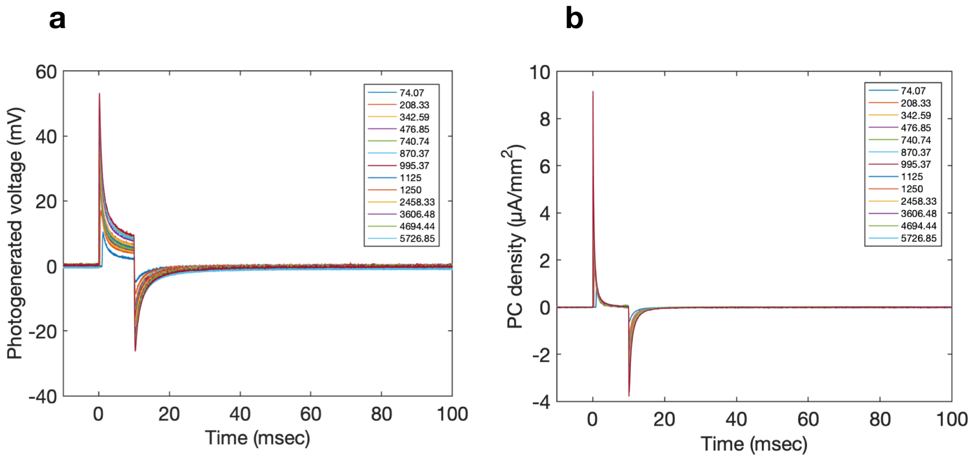

Figure 4.12: **a** Example of generated photovoltage and **b** example of generated PC density. The present measures have been collected on one cell with a diameter of 1000 µm at increasing LED intensities and pulse duration of 10 ms.

These disappointing results may arise for several causes. For instance, even though OSTE+ flex should be poorly permeable to gas, it could still be possible that a small amount of solvents get in contact with the photo-active polymers and denature them. On the other hand, given that few cells actually produced a photovoltaic response, the most realistic hypothesis is not related to OSTE+ flex permeability, but rather to the strong correlation between sputtered Ti films thickness and cracking of the same. As a consequence, we attribute the reason of such responses to this problem, which would, indeed, require further studies to be fixed or to be substituted by a completely different procedure for polymers patterning, for instance polymers printing. To conclude, during this study many microfabrication challenges have arisen. However, we have been able to solve the problems related to the electrodes and to integrate successfully OSTE+ CC and OSTE+ flex in the layout. Other challenges remain open, among them Ti sputtering and polymers etching.

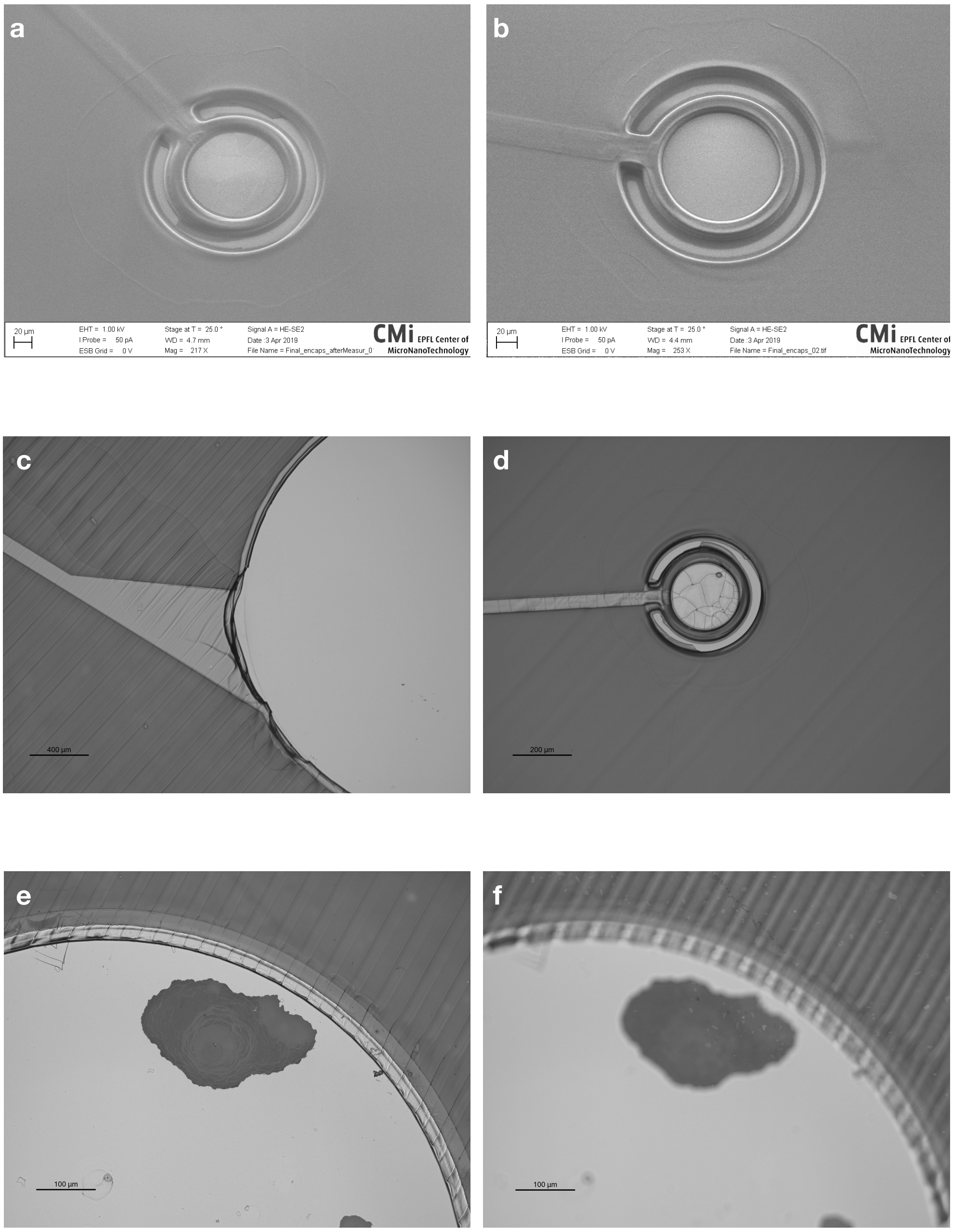

Figure 4.13: Batch 1: **a** SEM image taken at CMi (EPFL) with SEM Merlin by Zeiss depicting an uncomplete development of one electrode. In particular residual OSTE+ Flex can be noticed on the ring-shaped bottom anode. **b** SEM image taken at CMi (EPFL) with SEM Merlin by Zeiss depicting a complete development of OSTE+ Flex on one electrode. Both anode (bottom ring) and cathode (upper electrode) look totally clean from the encapsulation material. **c** Optical microscope image of a measurement pad taken after OSTE+ Flex (non-optimized) development in ethyl L-lactate for 4 minutes being shacked at 80rpm. OSTE+ Flex layer is detaching from the underlying layer. **d** Cracking of Ti top layer sputtered on OSTE+ Flex. **e**, **f** Ti detaching from a photovoltaic cell. Different focal planes to understand depth of detachment.

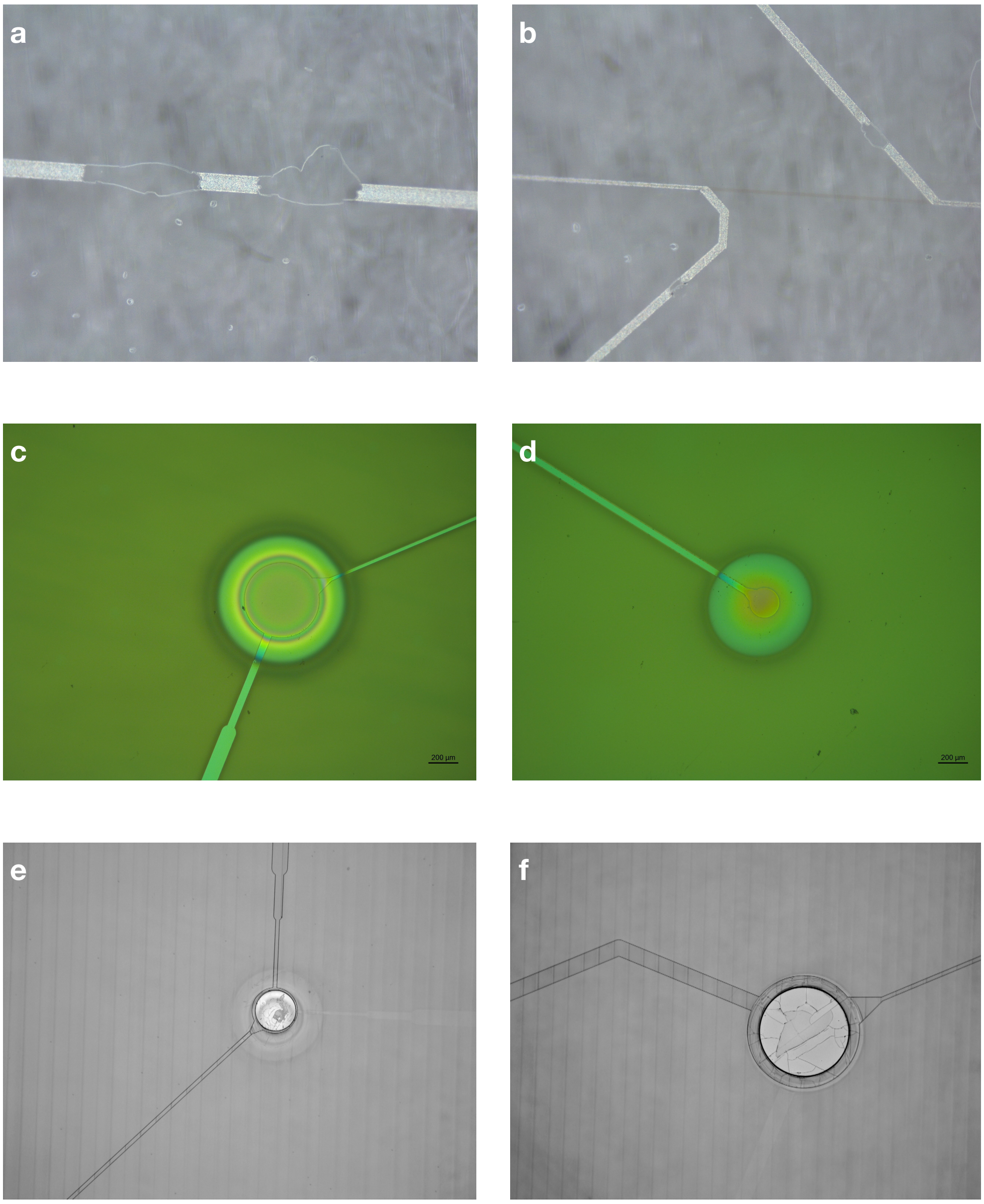

Figure 4.14: Batch 2 (optical microscope images): **a**, **b** Pt delamination from underlying OSTE+ Flex layer, plausibly due to a long-lasting lift-off plus sonication. **c**, **d** Sputtered Ti film through a shadow mask on two differently sized cells. The external shadow and the transparency of the film reveals that the real thickness of the coating is not the expected one (300 nm).**e**, **f** Ti top layer detachment on two differently sized cells due to bad coverage of Ti.

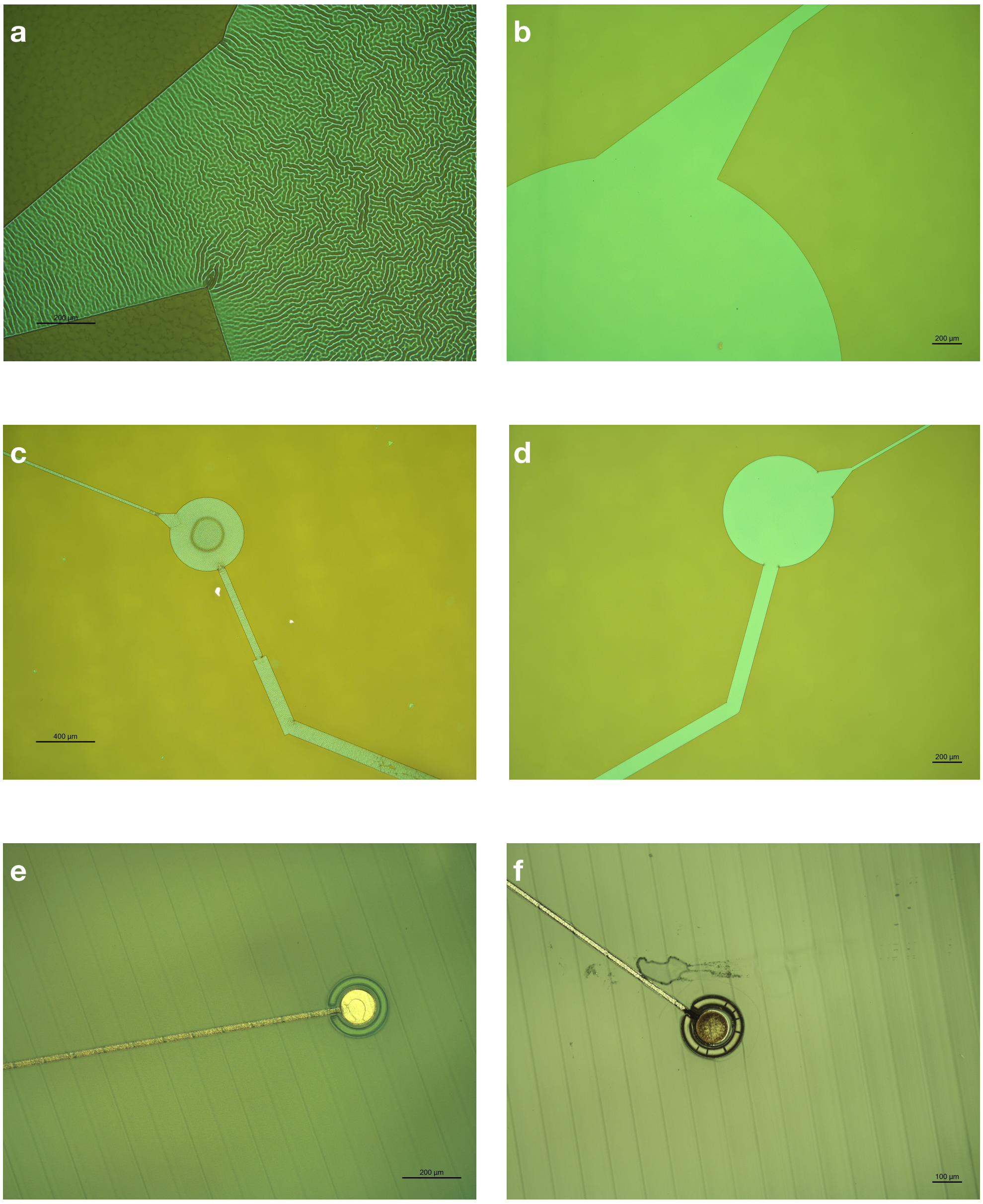

Figure 4.15: Batch 3 (optical microscope images): **a** ITO measurement pad deposited and patterned onto OSTE+ CC substrate. The waviness of the surface is due to the collapsing of ITO structures below OSTE+ CC in turn caused by inhomogeneous thermal curing. **b** A measurement pad successfully deposited and patterned onto OSTE+ CC. **c** Bottom electrode of a photovoltaic cell showing collapsing of structures below OSTE+ CC level aiming at showing that the collapse event does not depend upon structures size, but OSTE+ CC curing method. **d** Bottom electrode of a photovoltaic cell after OSTE+ CC curing standardization. **e** Pt electrode sputtered onto OSTE+ Flex. Lift-off process was shortened by implementing 2.5 µm AZ® 1512. **f** Unsuccessful IrOx sputtering and lift-off due to too high aspect ratio of electrodes after second encapsulation.

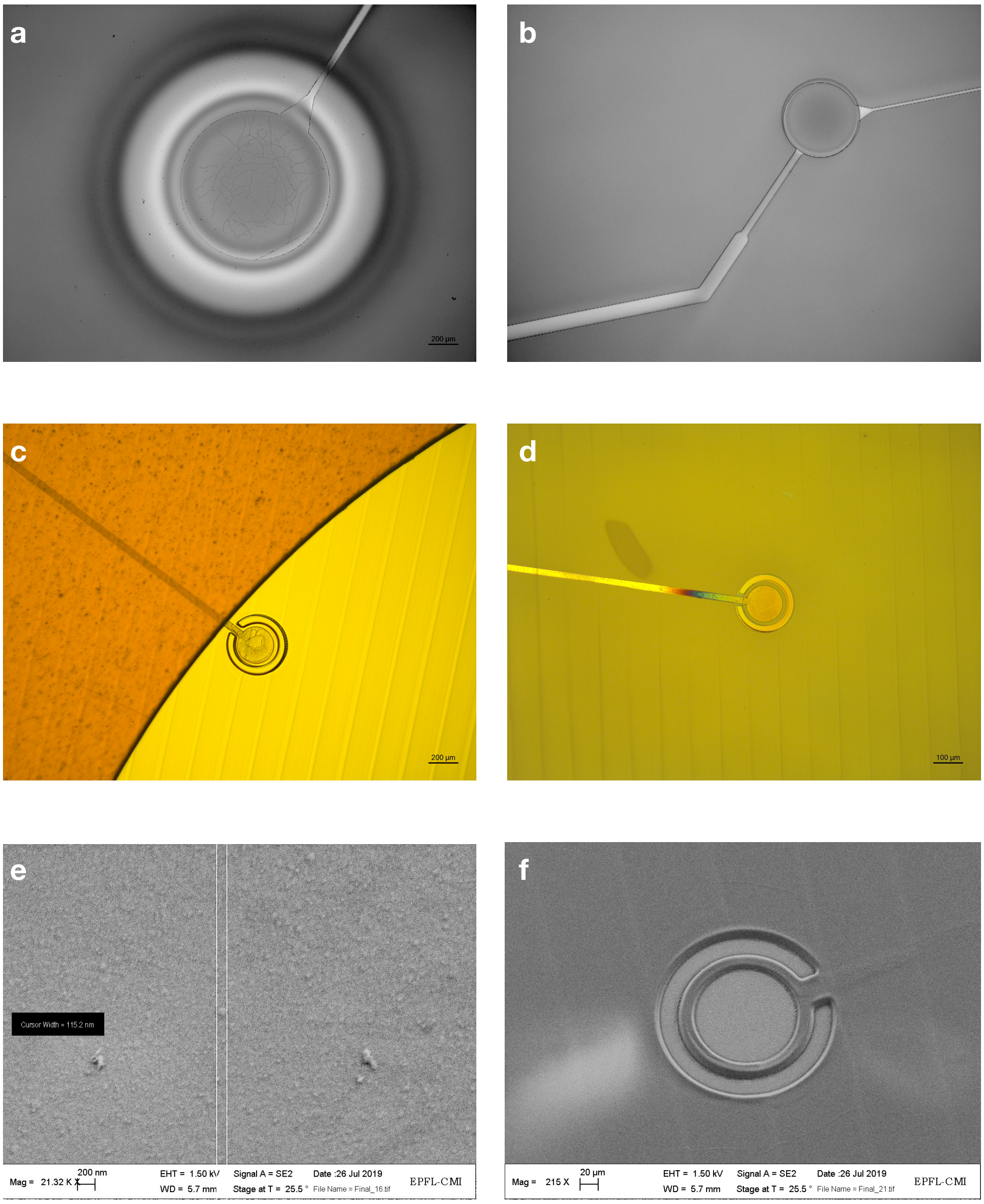

Figure 4.16: Batch 4: **a** Optical microscope image of sputtered Ti film through a shadow mask. The circular shadow is sign of unsuccessful Ti sputeering due to mask bending. **b** Optical microscope image of sputtered Ti film through a shadow mask. A good adhesion of the mask endowed a thick, uniform film. **c** Optical microscope image of shadow mask alignment for IrOx sputtering on Pt sputtered layer. **d** Optical microscope image of Pt and SIROF electrodes after lift-off. **e** SEM image of SIROF surface. **f** SEM image of SIROF-coated electrode.

5 Conclusion and future developments

The purpose of this project was to investigate the fabrication and the materials suitable for an organic photovoltaic cells array connected to stimulation electrodes in order to substitute IPGs, towards a mini-invasive and flexible visual, but not only, neuroprosthesis. In particular, at this stage the study has been performed with the final aim of integrating such photovoltaic technology with OpticSELINE [1]. Even though this objective still requires great effort to be achieved, this intermediate study helped to bring the idea into a first prototype and to pave the way for following investigations. Throughout this thesis, we have first explored all the possible organic solar cells configurations. BHJ approach has been chosen due to its ultrafast exciton separation given by the interpenetration of the electron acceptor and electron donor materials. Subsequently, we have investigated the state-of-the-art conjugated polymeric materials in order to be implemented as the electron donor material of an organic-based implantable photovoltaic cell. The requirement for minimal power loss due to skin absorption led us to opt for PCPDTBT, a narrow-bandgap polymer with a maximum of absorption peak at 770 nm. As a matter of fact, human skin is totally transparent to NIR and IR light, therefore working in this range of wavelengths reduces losses to a minimum.

One second issue related to implantable neuroprosthesis is the compliance of the final device. In order to avoid foreign body reaction and fibrotic capsule formation, which in turn causes electrical properties degradation, the devices should be embedded in a polymeric flexible substrate and encapsulation mimicking the targeted tissues mechanical behaviour. For this reason, we have studied and successfully integrated the photovoltaic system and electrodes with relatively novel materials: OSTE+ CC and OSTE+ flex. Along with their outstanding mechanical properties, OSTE+ polymers ensure optical transparency to a broad range of light frequencies, which is a desirable property when dealing with PV cells.

Preliminary studies have been performed on test chips representing a simplified version of the photovoltaic cells under study in order to set a benchmark for the following analysis. For maximum value of irradiance of the 730 nm LED, or $5727\,\mathrm{mWmm^{-2}}$, we obtained a photo-voltage equal to $73.37 \pm 19.49\,\mathrm{mV}$. While the peak of current density at the highest irradiance was found to be $44.22 \pm 12.17\,\mu\mathrm{Amm^{-2}}$. The design of the photovoltaic system was then traduced into a process flow and in the end practically fabricated in the cleanroom facilities of Campus Biotech and CMi. The microfabrication procedure encountered numerous challenges, mostly related to the integration of the OSTE+ polymers with standard microfabrication processes. Most of them could be solved within the time of this study. For example, the development of OSTE+ flex was optimized in order to exposed the entire area of the electrodes to the electrolyte. The curing procedure of OSTE+ CC has been standardized to allow further material deposition onto it.

Moreover, the electrodes were successfully sputtered with a IrOx coating (SIROF) and enhanced CSCs were measured. All the devices have been electrochemically characterized through impedance spectroscopy and cyclic voltammetry in order to assess or deny the success of the microfabrication steps.

At the end of this work many challenges remain unsolved and request for further analysis. The most crucial is related to titaniun sputtering which is now carried out exploiting a shadow mask. The small features and the thickness of the mask prevent the metal to enter and deposit in a 300 nm thick and uniform layer. In order to overcome this problem a dedicated holder could be fabricated in order to compress the mask towards the wafer and prevent the occurrence of "clouding" effect. Such an holder should be fabricated in accordance with the specific sputtering system specifications. One other topic that could be tackled is related to polymers patterning. Ti sputtering and etching is required for selectively remove the polymers. However, this technique could cause over-etching of the substrate and it is strongly dependant upon sputtered Ti features resolution. One plausible solution to bypass the etching step could be to research a manner to directly print the polymers on the cells area, as it is already done for PEDOT:PSS [45]. In addition, inkjet-printing of the polymers would allow to automatize the film deposition, which is now user-dependant, and in the future to enable the transition to a larger scale of production.

From the point of view of the integration with OpticSELINE, or other peripheral nerve stimulation interfaces, the demand for a high resolution stimulation would require to embed a high number of photovoltaic cells in a matrix contained in small area, in order to match the number of stimulating electrodes. Once achieved such level of optimization and reliability of the device, it would be interesting to validate its functioning in animal models, for instance in rabbits optic nerve, as for OpticSELINE.

Bibliography

[1] V. Gaillet, A. Cutrone, F. Artoni, P. Vagni, A. M. Pratiwi, S. A. Romero, D. Lipucci di Paola, S. Micera, and D. Ghezzi, "Spatially selective activation of the visual cortex via intraneural stimulation of the optic nerve," *Nature Biomedical Engineering*, 2019.

[2] D. Zhou and E. Greenbaum, *Implantable Neural Prostheses 1: Devices and Applications*. 2009.

[3] L. Ferlauto, M. J. I. Airaghi Leccardi, N. A. L. Chenais, S. C. A. Gilliéron, P. Vagni, M. Bevilacqua, T. J. Wolfensberger, K. Sivula, and D. Ghezzi, "Design and validation of a foldable and photovoltaic wide-field epiretinal prosthesis," 2018.

[4] V. S. Mallela, V. Ilankumaran, and N. Srinivasa Rao, "Technical Series Trends in Cardiac Pacemaker Batteries," 2004.

[5] L. Timmermann, F. Hertel, and R. Eleopra, "A New Rechargeable Device for Deep Brain Stimulation : A Prospective Patient Satisfaction Survey," 2013.

[6] J. P. Kolcun and M. Y. Wang, "Subcutaneous Solar Cells Harvest Energy for Pulse Generation," 2017.

[7] F. Cicoira and S. Zhang, "Flexible self-powered biosensors," 2018.

[8] G. Polino, C. Lubrano, G. Ciccone, and F. Santoro, "Photogenerated Electrical Fields for Biomedical Applications," pp. 1–6, 2018.

[9] T. F. O. Connor, S. Savagatrup, and D. J. Lipomi, "Soft Power : Stretchable and Ultra-Flexible Energy Sources for Wearable and Implantable Devices," pp. 69–82, 2016.

[10] J. G. Betts, P. Desaix, E. Johnson, J. E. Johnson, O. Korol, D. Kruse, B. Poe, J. A. Wise, M. Womble, and K. A. Young, *Anatomy and Physiology*. Houston, Texas: OpenStax, 2017.

[11] C. Molnar and J. Gair, *CONCEPTS OF BIOLOGY-1st Canadian Edition*, vol. 01. BC-campus, 2015.

[12] "World report on vision." https://www.who.int/blindness/vision-report/wrv-info/en/. Accessed: 2019-07-11.

[13] R. R. A. Bourne, S. R. Flaxman, T. Braithwaite, M. V. Cicinelli, A. Das, J. B. Jonas, J. Keeffe, J. H. Kempen, J. Leasher, H. Limburg, K. Naidoo, K. Pesudovs, S. Resnikoff, A. Silvester, G. A. Stevens, N. Tahhan, T. Y. Wong, and H. R. Taylor, "Magnitude , temporal trends , and projections of the global prevalence of blindness and distance and near vision impairment: a systematic review and meta-analysis," *Lancet Glob Health*, 2017.

[14] Y. H. Luo and L. da Cruz, “The Argus ® II Retinal Prosthesis System,” *Progress in Retinal and Eye Research*, vol. 50, pp. 89–107, 2016.

[15] R. M. Mirochnik and J. S. Pezaris, “Contemporary approaches to visual prostheses,” *Military Medical Research*, vol. 9, pp. 1–9, 2019.

[16] B. P. Christie, M. Freeberg, W. D. Memberg, G. J. C. Pinault, H. A. Hoyen, D. J. Tyler, and R. J. Triolo, “Long-term stability of stimulating spiral nerve cuff electrodes on human peripheral nerves,” *Journal of NeuroEngineering and Rehabilitation*, pp. 1–12, 2017.

[17] A. Cutrone, J. Del Valle, D. Santos, J. Badia, C. Filippeschi, S. Micera, X. Navarro, and S. Bossi, “A three-dimensional self-opening intraneural peripheral interface (SELINE),” *Journal of Neural Engineering*, vol. 12, 2015.

[18] S. P. Lacour, G. Courtine, and J. Guck, “Materials and technologies for soft implantable neuroprostheses,” *Nature Reviews*, 2016.

[19] “MIT materials properties database: Polyimide.” http://www.mit.edu/ 6.777/matprops/polyimide.htm. Accessed: 2019-03-15.

[20] “MIT materials properties database: PDMS.” http://www.mit.edu/ 6.777/matprops/pdms.htm. Accessed: 2019-03-15.

[21] C. F. Carlborg, T. Haraldsson, and K. Oberg, “Lab on a Chip Beyond PDMS : off-stoichiometry thiol-ene (OSTE) based soft lithography for rapid prototyping of microfluidic devices,” *The Royal Society of Chemistry: Lab on a chip*, pp. 3136–3147, 2011.

[22] C. K. Jeong, K. I. Park, J. H. Son, G. T. Hwang, S. H. Lee, D. Y. Park, H. E. Lee, H. K. Lee, M. Byun, and K. J. Lee, “Self-powered fully-flexible light-emitting system enabled by flexible energy harvester,” *The Royal Society of Chemistry: Energy and Environmental Science*, vol. 7, pp. 4035–4043, 2014.

[23] C. Dagdeviren, B. D. Yang, Y. Su, P. L. Tran, P. Joe, E. Anderson, J. Xia, V. Doraiswamy, B. Dehdashti, X. Feng, B. Lu, R. Poston, Z. Khalpey, R. Ghaffari, Y. Huang, M. J. Slepian, and J. A. Rogers, “Conformal piezoelectric energy harvesting and storage from motions of the heart, lung, and diaphragm,” *Proceedings of the National Academy of Sciences*, vol. 111, pp. 1927–1932, 2014.

[24] J. Olivo, S. Carrara, and G. D. Micheli, “Energy Harvesting and Remote Powering for Implantable Biosensors,” *IEEE sensors journal*, vol. 11, pp. 1573–1586, 2011.

[25] S. Ayazian, V. A. Akhavan, E. Soenen, and A. Hassibi, “A photovoltaic-driven and energy-autonomous cmos implantable sensor,” *IEEE Transactions on Biomedical Circuits and Systems*, vol. 6, pp. 336–343, 2012.

[26] E. Moon, D. Blaauw, and J. D. Phillips, “Subcutaneous Photovoltaic Infrared Energy Harvesting for Bio-implantable Devices,” *IEEE Transactions on Electron Devices*, vol. 64, pp. 2432–2437, 2017.

[27] J. A. Fan, W. H. Yeo, Y. Su, Y. Hattori, W. Lee, S. Y. Jung, Y. Zhang, Z. Liu, H. Cheng, L. Falgout, M. Bajema, T. Coleman, D. Gregoire, R. J. Larsen, Y. Huang, and J. A. Rogers, “Fractal design concepts for stretchable electronics,” *Nature Communications*, vol. 5, pp. 1–8, 2014.

[28] S. P. Lacour, J. Jones, S. Wagner, T. Li, and Z. Suo, “Stretchable Interconnects for Elastic Electronic Surfaces,” *Proceedings of the IEEE*, vol. 93, pp. 1459–1467, 2005.

[29] K. Song, J. Hyun, H. Chae, K. Il, and J. Lee, “Generation of electrical power under human skin by subdermal solar cell arrays for implantable bioelectronic devices,” *Biosensors and Bioelectronics*, vol. 92, pp. 364–371, 2017.

[30] M. Kaltenbrunner, M. S. White, E. D. Głowacki, T. Sekitani, T. Someya, N. S. Sariciftci, and S. Bauer, “Ultrathin and lightweight organic solar cells with high flexibility,” *Nature Communications*, vol. 3, 2012.

[31] R. Hoffmann, C. Janiak, and C. Kollmar, “A Chemical Approach to the Orbitals of Organic Polymers,” *ACS publications Macromolecules*, vol. 24, pp. 3725–3746, 1991.

[32] W. C. H. Choy, *Organic Solar Cells Materials and Device Physics.* London: Springer, 2012.

[33] C. Yan, S. Barlow, Z. Wang, H. Yan, A. K. Jen, S. R. Marder, and X. Zhan, “Non-fullerene acceptors for organic solar cells,” *Nature Publishing Group*, vol. 3, pp. 1–19, 2018.

[34] J. O. Bockris, A. K. N. Reddy, and M. Gamboa-Aldeco, *Modern electrochemistry Volume 2A - Fundamentals of Electrodics.* 2nd ed., 2000.

[35] D. T. Brocker and W. M. Grill, *Principles of electrical stimulation of neural tissue*, vol. 116. Elsevier B.V., 1 ed., 2013.

[36] T. Flores, G. Goetz, X. Lei, and D. Palanker, “Optimization of return electrodes in neurostimulating arrays,” *Jornal of Neural Engineering*, vol. 13, 2016.

[37] P. Li, J. Ouyang, F. H. Isikgor, D. Du, S. Zhang, X. Zhang, Y. Xia, and K. Sun, “Review on application of PEDOTs and PEDOT:PSS in energy conversion and storage devices,” *Journal of Materials Science: Materials in Electronics*, vol. 26, pp. 4438–4462, 2015.

[38] S. Han, M. Berggren, X. Crispin, S. Braun, S. Wang, A. Håkansson, M. Fahlman, J. Lu, and S. Fabiano, “Effect of (3-glycidyloxypropyl) trimethoxysilane (GOPS) on the electrical properties of PEDOT:PSS films,” *Journal of Polymer Science Part B: Polymer Physics*, vol. 55, pp. 814–820, 2017.

[39] D. Mühlbacher, M. Scharber, M. Morana, Z. Zhu, D. Waller, R. Gaudiana, and C. Brabec, “High Photovoltaic Performance of a Low-Bandgap Polymer,” *Advanced Materials*, vol. 01852, pp. 2884–2889, 2006.

[40] P. Vanlaeke, A. Swinnen, I. Haeldermans, and G. Vanhoyland, “P3HT/PCBM bulk heterojunction solar cells: Relation between morphology and electro-optical characteristics,” *Solar Energy Materials and Solar Cells*, vol. 90, pp. 2150–2158, 2006.

[41] C. F. Carlborg, A. Vastesson, Y. Liu, W. V. D. Wijngaart, M. Johansson, and T. Haraldsson, “Functional Off-Stoichiometry Thiol-ene-epoxy Thermosets Featuring Temporally Controlled Curing Stages via an UV/UV Dual Cure Process,” *Journal of Polymer Science Part A: Polymer chemistry*, pp. 2604–2615, 2014.

[42] S. F. Cogan, “Neural Stimulation and Recording Electrodes,” *Annual Review of Biomedical Engineering*, vol. 10, pp. 275–309, 2008.

[43] "Mercene Labs: OSTE crystal clear datasheet." http://www.ostemers.com/wp-content/uploads/2014/07/Product-sheet-OSTEMER™-322-Crystal-Clear1.pdf. Accessed: 2019-03-02.

[44] "Mercene Labs: OSTE flex datasheet." https://www.ostemers.com/wp-content/uploads/2016/11/Data-sheet-OSTEMER-324-Flex.pdf. Accessed: 2019-04-06.

[45] S. Hun, S. Senthilarasu, P. Uthirakumar, S. Cheol, J. Lim, C. Lee, H. Seok, J. Lee, and S. Lee, "Polymer solar cells based on inkjet-printed PEDOT:PSS layer," *Organic Electronics*, vol. 10, pp. 536–542, 2009.

6 Appendix

6.1 PEDOT:PSS + GOPS preparation

Reagents:

- Clevios ^{TM} PH 1000 by Heraeus
- GOPS

Workplace:

- Wetbench (lab) + hood

Procedure:

After having accurately shacked the PH 1000 bottle, with the help of a micropipette pour approximately 25 mL of PH 1000 in a 30 mL glass vial. Sonicate for 10 minutes at ambient temperature. Using a 5 µm PTFE filter and a syringe, filter the sonicated PH 1000 in a new glass vial. Then prepare one other glass vial with 20 mL of the filtered PH 1000 and add 0.1% of GOPS. Sonicate again for 20 minutes. After sonication, filter the solution with a 0.45 µm hydrophilic filter in a new vial. The solution must be stored at 8 °C

6.2 PCPDTBT + $PC_{60}BM$ (blend) preparation

Reagents:

- PCPDTBT by Sigma-Aldrich®
- $PC_{60}BM$
- Chlorobenzene by Sigma-Aldrich®

Workplace:

- Glovebox (cleanroom)

Procedure:

In a glass vial weight 20 mg of PCPDTBT, then add 1 mL of chlorobenzene (usual concentration 20mg/mL). Place the vial on the hotplate set at 70°C under continuous stirring overnight. The same procedure and quantity of reagents can be implemented for

the $PC_{60}BM$. Once the reagents have been prepared, take a new glass vial and pour the two regents in a 1:1 proportion in volume. Before mixing remember to filter both solutions with a 0,45 um PTFE filter. Put the solution on the hotplate at 70°C for 3 minutes then let it cool down while keeping under continuous stirring.
The solution can be stored in nitrogen atmosphere for approximately 3 to 4 weeks under stirring.

6.3 OSTE+ flex preparation

Reagents:

- OSTEMER® 324 Flex component A
- OSTEMER® 324 Flex component B

Workplace:

- Wetbench (PDMS zone cleanroom) + hood

Procedure:

Implementing a balance and a Pasteur pipette measure the amount of B component which is needed. For spin coating a layer of 5 µm circa, 3 grams are a suitable quantity. Then add the component A respecting the ratio of 1:1.24. Mix accurately, this step can be done manually or implementing a mixer. After having been mixed OSTE+ flex is ready for being spincoated over wafers and then exposed for photolithographic purposes.

6.4 OSTE+ CC preparation

Reagents:

- OSTEMER™ 322 Crystal Clear component A
- OSTEMER™ 322 Crystal Clear component B

Workplace:

- Wetbench (PDMS zone cleanroom) + hood

Procedure:

Implementing a balance and a Pasteur pipette measure the amount of B component which is needed. For spin coating a layer of 5 µm circa, 3 grams are a suitable quantity. Then add the component A respecting the ratio of 1:1.09. Mix accurately, this step can be done manually or implementing a mixer. After having been mixed OSTE+ CC is ready for being spincoated over wafers and then exposed for photolithographic purposes.